THE ASTROPHYSICAL JOURNAL, 446:665–686, 1995 June 20

THE LINE WIDTH–SIZE RELATION IN MASSIVE CLOUD CORES

P. CASELLI AND P. C. MYERS
Harvard-Smithsonian Center for Astrophysics, 60 Garden Street, Cambridge, MA 02138
Received 1994 February 28; accepted 1994 December 29

ABSTRACT

We report ^{13}CO and $C^{18}O$ line observations and maps in Orion A (L1641) and B (L1630). Together with already published observations, these data are used to study the line width–map size relation in massive star-forming regions. The nonthermal component of the line width (Δv_{NT}) in Orion cores follows the trend $\Delta v_{NT} \sim R^q$ with $q = 0.21 \pm 0.03$, significantly different from $q = 0.53 \pm 0.07$ found in low-mass cores. These relations are analyzed in the context of an equilibrium model of a spherically symmetric dense core which incorporates both thermal and nonthermal ("TNT") motions. The internal consistency of the TNT model and Δv_{NT}–R data is shown. We present general formulae for the TNT model and apply them to the observational data. Differences in the slope and in the intercept of the log Δv_{NT}–log R relation between massive and low-mass cores imply significant differences in density structure, pressure profile, mass infall rate, and probably in the masses of stars which form. In particular, massive cores are denser and have steeper density profiles than low-mass cores. Visual extinction values predicted by the TNT model for low mass and massive cores (3.3 and 16 mag, respectively) are in good agreement with available observational estimates for similar objects. The higher density and pressure in massive cores lead to values for the infall time for 1 $M_\odot$ of $\sim 7 \times 10^4$ yr, ~ 6 times shorter than in low-mass cores. Massive dense cores associated with embedded young stellar objects have physical properties almost identical to neighboring massive starless cores. Thus, the formation of a star or a small group of stars does not significantly affect the initial physical conditions of the associated molecular cloud core. On the other hand, line widths of ammonia cores become narrower as the distance from embedded young stellar clusters increases. In particular, the massive core farthest away from embedded clusters is mostly thermal and its kinetic temperature is ~ 10 K, ~ 2 times lower than the typical kinetic temperature of massive cores.

Subject headings: ISM: clouds — ISM: kinematics and dynamics — ISM: molecules — stars: formation

1. INTRODUCTION

An important aspect of the physical conditions in star-forming molecular clouds is the spatial distribution of internal motions and support. It has long been known that Δv_{obs}, the FWHM velocity width of a line observed in a particular cloud, and R, the size of the half-maximum (HM) contour map of the intensity of the same line, correlate from line to line in a given cloud (Ho et al. 1977; Myers et al. 1978; Snell 1980; Larson 1981), and that for most lines the width is dominated by nonthermal, supersonic motions. The physical basis of the relationship is still poorly understood, although the line broadening is probably magnetic in origin (Myers & Goodman 1988; Goodman et al. 1989). Only recently have enough mapping data become available to allow comparisons between clouds, and to interpret the Δv_{obs}–R relation in terms of models of cloud structure and evolution.

Fuller & Myers (1992, hereafter FM) reported observations of 14 low-mass cores, each in lines of NH_3, CS, and $C^{18}O$. The observed line widths follow the trend $\Delta v_{obs} \sim R^q$, with $q = 0.44 \pm 0.08$ for six "starless" cores and $q = 0.4 \pm 0.1$ for eight cores with associated stars, of median luminosity 2 $L_\odot$. Thus the slope of the line width–size relation appears independent of the presence of associated stars, and the physical conditions underlying this relation can be considered part of the initial conditions of the star formation process.

According to the small amount of evidence now available, regions forming massive stars have broader lines, and shallower line width–size relations than do regions forming low-mass stars. The slope q on a log-log plot of the nonthermal component of the line width Δv_{NT} versus the map size R is 0.65 ± 0.08 for the 14 low-mass cores of FM, 0.5 ± 0.1 for the tcore in L1204 associated with the H II region S140, and is 0.28 ± 0.03 for the core in the ρ Oph dark cloud associated with the well-known embedded cluster of some 80 stars (Myers & Fuller 1992, hereafter MF).

In this paper we present a new well-defined line width size relation in massive cloud cores deduced from a literature search on Orion Molecular Cloud cores combined with new observations in ^{13}CO and $C^{18}O$ in the same region. Each core has been mapped in at least three different molecular lines, $NH_3(1, 1)$, $CS(2 \rightarrow 1)$ or $CS(1 \rightarrow 0)$, and $^{13}CO(1 \rightarrow 0)$. These molecular species trace physical conditions from size scales of a few hundredths of a parsec to ~ 1 pc. The same range of observational data is available for low-mass cores, after the inclusion of new ^{13}CO observations (Fukui & Mizuno 1992) in the dense cores studied by FM; this allows a fair comparison of physical properties in massive and low-mass cores deduced from observations, and their interpretation in the context of a spherically symmetric cloud in hydrostatic equilibrium (HSE) with thermal and nonthermal motions (the "TNT" model introduced by MF). Closely related studies have been carried out by Holliman & McKee (1994), who model the Δv-R relation reported in this paper as arising from pressure associated with magnetic fields and Alfvén waves.

In § 2 we describe how we selected the sample of massive cores from the literature and our new observations. In § 3 we define "size" and "line width" and we present the results of the literature search and observations. In § 4 the new line width–size relation in massive cores is shown and compared with that relative to low-mass cores. Section 5 presents general

formulae for the HSE model, and its application to the data to deduce density structure, pressure profiles, and mass infall rates in massive and low-mass cores. In § 6, we discuss the effects of embedded stars on the initial physical conditions of star-forming molecular cloud cores. Section 7 summarizes the paper.

2. THE SELECTION OF THE MASSIVE CORE SAMPLE

2.1. *The Literature Search*

The Orion Molecular Cloud is the nearest and one of the best-studied regions forming massive stars (for a detailed review, see Genzel & Stutzki 1989). We focused our study on this region to better define the line width–map size relation in massive cores. We carried out a literature search on Orion cores primarily using the Brand & Wouterloot (1991) catalog. As selection criteria we required that each core has been mapped at least in two different molecular lines, and that the half-maximum contour maps significantly overlap in space. We also restricted the angular resolution ($\Delta\theta$) of the selected maps to values $\leq 1'.8$ for high-density molecular tracers, such as CS and NH_3, and $\leq 2'.7$ for larger scale maps, such as ^{13}CO maps. The first $\Delta\theta$ upper limit comes from the CS(2 – 1) survey in Orion B by Lada, Bally, & Stark (1991, hereafter LBS); the $\Delta\theta$ upper limit relative to larger scale maps refers to $^{13}CO(1-0)$ observations in Orion A from Sugitani et al. (1986, hereafter SFOK).

We did not include the more extended large-scale surveys in H I by Green (1990), in OH by Baud & Wouterloot (1980), in $^{12}CO(1 \rightarrow 0)$ by Maddalena et al. (1986), and in H_2CO by Cohen et al. (1983) because of their coarse angular resolution compared with the well-resolved small-scale tracer maps. We did not consider cores close to the BN-KL infrared nebula and the OMC-1 molecular cloud, where the presence of intense UV fields, strong winds, and outflows driven by massive stars may strongly affect the structure and physical properties of the surrounding molecular environment.

Finally, we did not include in our analysis interferometric observations, which concern much smaller size scales than single-dish observations. VLA maps of $NH_3(1, 1)$ have been done in several high-mass star-forming regions. In particular, Zhou, Evans, & Mundy (1990, hereafter ZEM) used the VLA to observe $NH_3(1, 1)$ and (2, 2) in NGC 2071 in Orion B. The region they observed is centered on one of the near-infrared clusters discovered by Lada et al. (1991) during their unbiased survey at 2.2 μm in Orion B. Therefore the mapped gas is strongly affected by the embedded young stars which drive a powerful, well-collimated outflow seen in CO (Snell et al. 1984), CS (Takano et al. 1984), and HCO^+ (Wootten et al. 1984). In fact, the results of ZEM indicate that the NH_3 emission is distributed in a ring about the infrared sources and the dense core, instead of tracing the dense core. Here the authors are probably seeing a more evolved phase of a star-forming ammonia core, when the newly born stars already started the disruption of the circumstellar cloud. We point out that for the core size scales studied in this paper, where the effects on molecular line widths of embedded low- and moderate-luminosity stars are not significant (see § 6), NH_3 is indeed a good tracer of dense gas (densities $\sim 10^4$–10^5 cm^{-3}; e.g., Benson & Myers 1989). Moreover, other well-known tracers of dense gas, such as HC_3N, C_3H_2, and N_2H^+ give estimates of line width and size similar to those deduced from NH_3 maps of the same objects, both in low-mass (Fuller & Myers 1993; Benson et al. 1994) and massive (Caselli & Myers 1994) cores.

In the present study we avoid the analysis of complex regions, such as OMC-1 or the NGC 2071 cluster region; we concentrate our attention on star-forming dense cores where the effects of embedded stars are not yet detectable (see § 6).

Several molecular condensations in L1630 (Orion B) have been mapped in CS by LBS, in NH_3 by Harju, Walmsley, & Wouterloot (1993, hereafter HWW), and Iwata, Fukui, & Ogawa (1988, hereafter IFO); we have very little information about $C^{18}O$ (just two coarse angular resolution maps by IFO: one in NGC 2071 North and one in NGC 2071) and no available information about the ^{13}CO distribution with the exception of a map showed but not discussed by Bally (1989). Goldsmith et al. (1992, hereafter GMSF) show a ^{13}CO map in NGC 2071 North obtained with the FCRAO telescope, but they surveyed a limited region from which we cannot deduce size because the half maximum contour lies beyond the boundaries of the mapped region.

L1641 (Orion A) has been extensively mapped in CS by Tatematsu et al. (1993, hereafter TUKH), and we have also ammonia data from Bartla et al. (1983, hereafter BWBR), and HWW for cores associated with *IRAS* sources, and from Cesaroni & Wilson (1994, hereafter CW). ^{13}CO data are available from Bally et al. (1987, hereafter BLSW) and SFOK. Recent ^{13}CO maps in L1641 by Chen, Fukui, & Iwata (1993) are limited in extent and do not allow estimation of the core size. Again, in L1641 there are not available $C^{18}O$ line widths and sizes of individual cores, although the region has been mapped in the above molecule by Dutrey et al. (1991). Finally, if we do not consider the KL nebula and the BN object, a few single-dish observations of Orion cores have been made in other molecular lines (e.g., Chen, Fukui, & Young 1992 for HCO^+) from which we can deduce useful parameters.

To summarize, requiring that each core has been mapped with good angular resolution in at least two different molecules we collected 72 Orion cores. Sixteen of them (six in Orion B, and 10 in Orion A) have been mapped in three or more different molecular tracers, but seven out of 16 lack large-scale (~ 1 pc) maps such as in ^{13}CO. The other 56 cores have just two maps, 42 have been mapped in CS (TUKH), and they are embedded in ^{13}CO clouds (BLSW; SFOK), and 14 have been mapped in CS (LBS; TUKH), and NH_3 (BWBR; HWW; CW).

We decided to include in our sample cloud cores with at least three maps in different molecular tracers, including small-scale maps (e.g., in NH_3, CS) and larger scale maps such as in ^{13}CO. This criterion is necessary to have a well-defined line width–size relation, to compare the Δv–R relation of individual cores with each other, and to verify if the general Δv-R relation in massive cores is primarily due to the variation of line width with size within the cores in the sample rather than to any core-to-core variation, as it was found by FM for the case of low-mass cores. Because of the lack of available data in ^{13}CO and $C^{18}O$, especially in Orion B, we decided to map such molecules in selected parts of L1630 and L1641 containing cores already mapped in NH_3 and CS. These observations, described in the next section, have furnished new large-scale data for nine cores in Orion B and five cores in Orion A. The literature search together with our new observations yielded 24 Orion cores, each having at least three maps in different molecular lines.

2.2. *Observations*

The $J = 1 \rightarrow 0$ ^{13}CO and $C^{18}O$ observations were made in 1993 April and May at the FCRAO 14 m telescope at New Salem, Massachusetts. We used the 15 element QUARRY

receiver (Erickson et al. 1992) with a set of filterbanks each having 32 channels and a velocity resolution 0.686 km s^{-1} at 110 GHz. At this frequency, the typical system temperature (SSB) was ~600 K. The main beam width at half-power was 50″. The data were acquired in position-switching mode and calibrated using the ambient load vane method. The rms pointing error, estimated by observing SiO masers in Orion and planets, was ~5″. The main beam efficiency up to the half-power point was ~0.45 at the frequencies considered (Patel, Xie, & Goldsmith 1995). The rms noise in each channel was typically 0.2 K in ^{13}CO and 0.1 K in $C^{18}O$.

We completed four Nyquist sampled maps, three in ^{13}CO and one in $C^{18}O$, presented below in the form of contour maps in Figures 1, 3, and 5.

2.2.1. *Orion B*

The ^{13}CO contour map of integrated intensity in Orion B is shown in Figure 1. The three clouds in the figure are NGC 2071 North, NGC 2071, and NGC 2068 going from northeast to southwest. In NGC 2071 North the ^{13}CO half-maximum (HM) contour encloses four ammonia cores and one $C^{18}O$ core observed by IFO; in the same cloud GMSF observed HCO^+ and CS. Figure 2 shows a composite picture of this region; for each map the HM contour has been reported. The $C^{18}O$ observations have been carried out by IFO using the 4 m telescope at Nagoya University; they give just a rough estimate

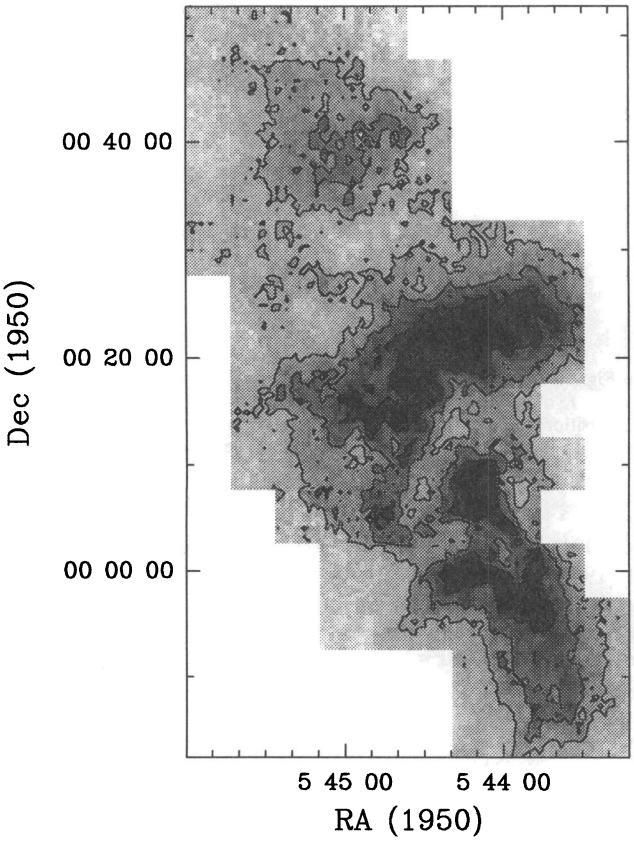

FIG. 1.—$^{13}CO(1–0)$ contour map of integrated intensity in Orion B. The spectra have been integrated over 7–12 km s^{-1}; the peak contour integrated intensity is 17 K km s^{-1}. The contour interval is 3 K km s^{-1} and ranges from 5 to 14 K km s^{-1}. The gray-scale ranges from −1 to 17 K km s^{-1} in equal steps of 0.2 K km s^{-1}. The three clouds in the figure are NGC 2071 North, NGC 2071, and NGC 2068 going from northeast to southwest.

of the line width for this cloud (~1.8 km s^{-1}). Therefore, to have a better estimate of Δv we observed $C^{18}O$ in selected positions of the $C^{18}O$ cloud mapped by IFO, in the center and in four positions on the HM contour, as it is shown in Figure 2. These observations have been made using the 3 mm receiver recently installed at the 37 m Haystack antenna; using the 17.8 MHz correlator bandwidth the velocity resolution of this system is ~0.04 km s^{-1}. The half-power beam width is ~25″, and the main beam efficiency was ~0.2 including the effect of the radome. The spectra were taken by using overlap frequency switching for integration times of 50 minutes.

From Figure 2 it is evident that the $C^{18}O$ line changes its shape and width across the cloud; the line in the center of the cloud (spectrum labeled "c") may be the blending of two components with almost the same intensity. The two components seem to vary inversely in intensity going from northeast (spectrum a in Fig. 2) to southwest (spectrum d) toward the clump. In particular, the higher velocity component becomes very narrow ($\Delta v \sim 0.4$ km s^{-1}) in the direction of position "a." At the size scales of $C^{18}O$ maps, this value is unusually low for massive star-forming regions, in which nonthermal motions generally dominate over the thermal ones (Myers, Ladd, & Fuller 1991). It could be interesting to map this region again with better angular resolution than that achieved by the 4 m telescope used by IFO and study in more detail the line width gradient toward NGC 2071 North. From our observations, as we will show in the next section, we deduced a new and maybe more accurate value of the line width relative to the $C^{18}O$ map in this cloud.

Both in NGC 2071 and NGC 2068 the ^{13}CO HM contour encloses two cores mapped in NH_3 (HWW) and CS (LBS). The cores in NGC 2071 lie in proximity of the infrared cluster observed in the 2.2 μm survey of Lada et al. (1991). The cores in NGC 2068 are close to the southern edge of the ^{13}CO HM contour at ~20′ from the infrared cluster embedded in this cloud (Lada et al. 1991).

2.2.2. *Ori B9*

Ori B9 is a relatively isolated cloud ~80′ southwest from NGC 2068 and ~40′ northeast from NGC 2024 (see Fig. 2 in LBS). ^{13}CO and $C^{18}O$ contour maps of integrated intensity, obtained at the FCRAO antenna, are in Figures 3*a* and 3*b*, respectively. To have a well-defined estimate of the ^{13}CO half-maximum contour we extended the map toward NGC 2024, whose northern edge is shown in the bottom left of Figure 3*a*; here the peak contour integrated intensity is 16 K km s^{-1}, ~2 times larger than in the Ori B9 cloud.

In Figure 4 the HM contours for the ^{13}CO and $C^{18}O$ maps are shown together with the NH_3 half-maximum contour maps from HWW and the associated *IRAS* sources whose positions are marked by stars in the figure. The two ammonia cores have been also mapped in CS by LBS. One interesting feature in this cloud is that the core at the northeastern edge of the ^{13}CO HM contour (Ori B9b), associated with IRAS 05405 − 0117 (whose infrared luminosity is 8 $L_\odot$), has the narrowest lines in both the NH_3 survey of HWW ($\Delta v_{obs} = 0.29$ km s^{-1}) and the CS survey of LBS ($\Delta v_{obs} = 0.56$ km s^{-1}); the kinetic temperature, deduced by ammonia observations has been found ~10 K. The physical properties of this core are very close to those of low-mass cores (Benson & Myers 1989). We did not detect any $C^{18}O$ core in the direction of this mostly thermal core, perhaps because of the velocity resolution (0.686 km s^{-1}) of the FCRAO antenna. However, a similar character-

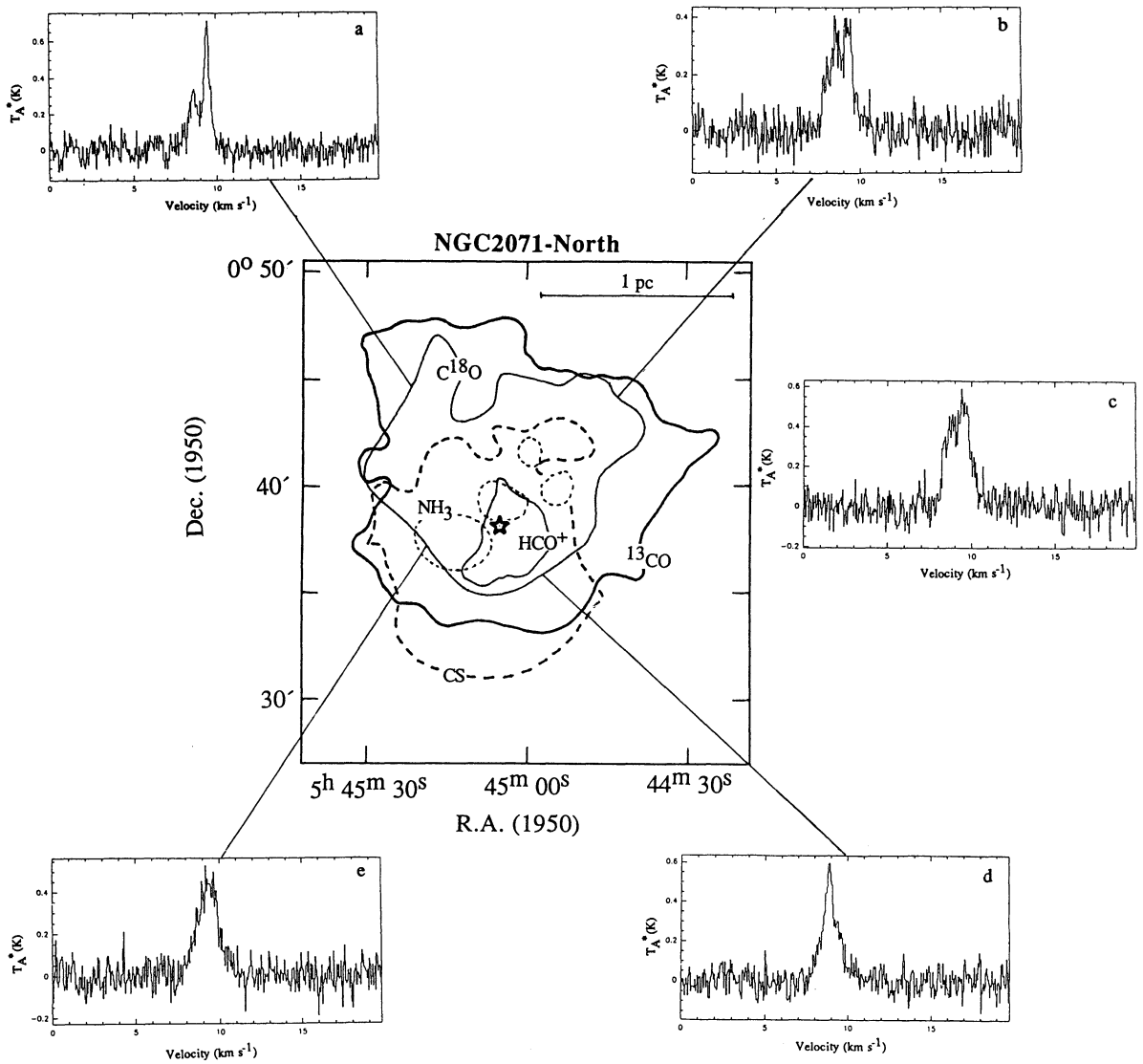

FIG. 2.—Composite view of half-maximum contour maps in ^{13}CO (our data; see Fig. 1), $C^{18}O$ and NH_3 (Iwata, Fukui, & Ogawa 1988), CS and HCO^+ (Goldsmith et al. 1992) for NGC 2071 North. The $C^{18}O$ spectra at the indicated positions were observed at the Haystack antenna using the new 3 mm receiver; the velocity scale is between 0 and 20 km s^{-1}. The spectrum labeled "c" refers to the central position of the $C^{18}O$ cloud. The $C^{18}O$ line is probably the blending of two components; the higher velocity component becomes unusually narrow ($\sim$0.4 km s^{-1}) toward position "a", at the northeast edge of the cloud.

istic has been found by Goldsmith et al. (1992) in NGC 2071 North, where three over four ammonia cores, observed by IFO, do not agree in position with local maxima of $C^{18}O$. The authors concluded that since there was no evidence for a column density peak in correspondence of ammonia cores, the most likely explanation is a significant increase of the NH_3 fractional abundance. Ori B9 needs to be investigated in more detail, both for a better understanding of the observed different morphologies of various molecular tracers, and to analyze in which particular environments and physical conditions quiescent dense cores form inside massive molecular clouds, typically associated with embedded primarily nonthermal cores (see discussion in § 6).

2.2.3. *Orion A*

Line widths and sizes for the ^{13}CO and $C^{18}O$ maps of the so-called "∫-shaped" streamer in Orion A, north of OMC-1, have not been published although this region has been mapped in ^{13}CO by BLSW, Castets et al. (1990), in $C^{18}O$ by Dutrey et al. (1991), in CS by TUKH, and in NH_3 by joining the Bartla et al. (1983) maps with recent observations by CW. Therefore we used the FCRAO antenna to map the ^{13}CO emission in this region of Orion A around six NH_3 (CW) *and* CS (TUKH) cores. The contour map of integrated intensity is shown in Figure 5. The map has been extended in the south to have a good estimate of the HM contour for the ^{13}CO emission, but, as we explained in § 2.1, we have not considered cores close to OMC 1 (centered at $\alpha(1950) = 5^h32^m46^s.3$, $\delta[1950] = -5°24'23''$; Bartla et al. 1983), i.e., all the cores embedded in the southern ^{13}CO condensation in Figure 5.

3. RESULTS

In the following two subsections we describe how we obtained line width and size estimates for the ^{13}CO and $C^{18}O$ clouds observed in this work and described in Section 2.2.

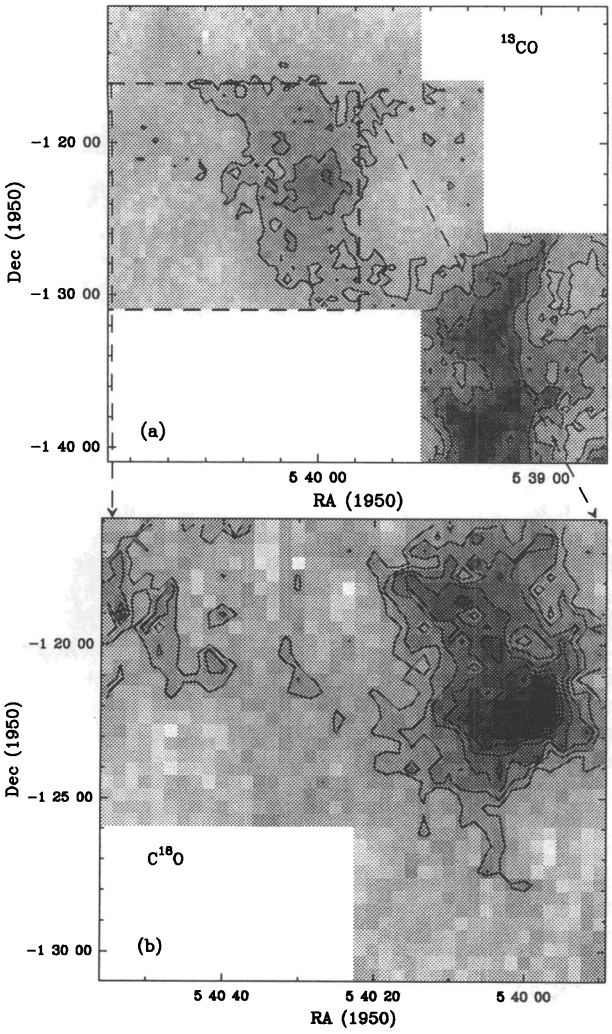

FIG. 3.—(*a*) ^{13}CO contour map of integrated intensity in Ori B9 (the northeast cloud in the figure). The spectra have been integrated over 7–11 km s^{-1}; the peak contour integrated intensity for the Ori B9 cloud is 8 K km s^{-1}; the contour interval is 2 K km s^{-1} and ranges from 4 to 8 K km s^{-1}. The gray scale ranges from −1 to 16 K km s^{-1} in equal steps of 0.2 K km s^{-1}. Toward the southwest, the northeastern edge of NGC 2024 is visible; here the peak contour flux is ~16 K km s^{-1}. (*b*) Integrated intensity map in C^{18}O(1–0) for the Ori B9 cloud. The spectra have been integrated over 8 to 10 km s^{-1}; the lowest contour is at 0.6 K km s^{-1}, the highest is at 2.2 K km s^{-1} and the contour spacing is 0.2 K km s^{-1}; the peak contour integrated intensity is 2.4 K km s^{-1}, and it is located very close to the ^{13}CO peak. The gray scale ranges from −0.4 to 2.4 K km s^{-1} in equal steps of 0.03 K km s^{-1}. The C^{18}O distribution in this cloud may be undersampled because the line width may be comparable to the spectrometer resolution (~0.7 km s^{-1}).

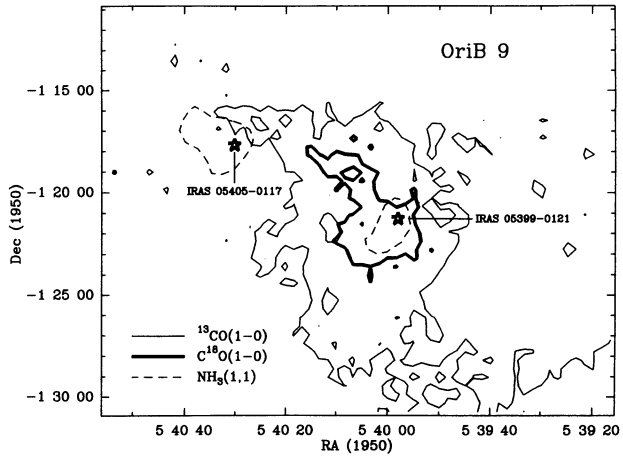

FIG. 4.—Overlay of the half-maximum contour maps in ^{13}CO and C^{18}O in Ori B9 (see Fig. 3). Half-maximum contours of ammonia maps (*dashed lines*) from Harju, Walmsley, & Wouterloot (1993; HWW) are shown together with the positions of the embedded *IRAS* sources, marked by stars. The core associated with IRAS 05405 − 0117 has the narrowest NH_3 line width in the HWW survey, and the narrowest CS line width in the Lada, Bally, & Stark (1991) survey; its physical properties are very close to low-mass cores (Benson & Myers 1989).

3.1. *Line Width Estimates*

3.1.1. *Mean Line Width*

To calculate the mean line width in every mapped cloud we considered all the spectra inside the corresponding half-maximum contour, the adopted boundary of the map (see § 3.2). For the ^{13}CO and C^{18}O observations made at the FCRAO antenna using the 3 mm QUARRY receiver, every observed position is associated with a grid of 30 spectra (called scan) spaced by 25″ (for the Nyquist sampling), which cover an area of ~2.′1 × 2.′6. Because of the extension of ^{13}CO maps (average area ~154 arcm^2; see § 3.2) each containing an average number of spectra of ~900, we considered individual scans, or groups of 30 spectra, inside the HM contour. If a scan was located at the boundary of the map, we excluded from the computation of the mean line width those spectra lying outside the HM contour. If more than $\frac{2}{3}$ of the spectra contained in a "boundary" scan lay outside (inside) the HM contour, we eliminated (included) the entire scan from the calculation, for the statistical significance of each scan (see the following discussion). This choice negligibly affected the final result. The same method has been applied for the C^{18}O map in Ori B9. We calculated the velocity dispersion for each spectrum i contained in the jth scan (σ_{vij}), using the second moment of the velocity profiles (van Gorkom & Ekers 1991):

$$\sigma_{vij} = [(\langle v^2\rangle_i)^{1/2}]_j = \left[\frac{\sum_{k=1}^{n} T^*_{Aki}(\alpha, \delta)(v_{ki} - \langle v_i\rangle)^2}{\sum_{k=1}^{n} T^*_{Aki}(\alpha, \delta)}\right]_j^{1/2}, \quad (1)$$

where $T^*_{Aki}(\alpha, \delta)$ is the antenna temperature corrected for atmospheric attenuation, at velocity v_{ki} and position (α, δ), n is the total number of channels over which the spectra have been integrated and $\langle v_i\rangle$ is the intensity weighted mean velocity for the ith spectrum:

$$\langle v_i\rangle = \left[\frac{\sum_{k=1}^{n} T^*_{Aki}(\alpha, \delta) v_{ki}}{\sum_{k=1}^{n} T^*_{Aki}(\alpha, \delta)}\right] \quad (2)$$

This calculation was computed using the NRAO-AIPS software package, which furnished the mean value ($\langle\sigma_{vj}\rangle$) of the velocity dispersion in each group of spectra, and the relative dispersion σ_j. Then we calculated the mean line width $\langle\Delta v\rangle$ and the associated error for each cloud multiplying the cloud mean velocity dispersion ($\langle\sigma_v\rangle$) and the associated error ($\sigma_{\langle\sigma v\rangle}$) by $(8 \ln 2)^{1/2}$, where

$$\langle\sigma_v\rangle = \frac{\sum_{j=1}^{N} (\langle\sigma_{vj}\rangle/\sigma_j^2)}{\sum_{j=1}^{N} (1/\sigma_j^2)}, \quad (3)$$

$$\sigma_{\langle\sigma v\rangle} = [\textstyle\sum_{j=1}^{N} (1/\sigma_j^2)]^{-1/2} \quad (4)$$

In equation (3) N is the number of scans inside the HM contour.

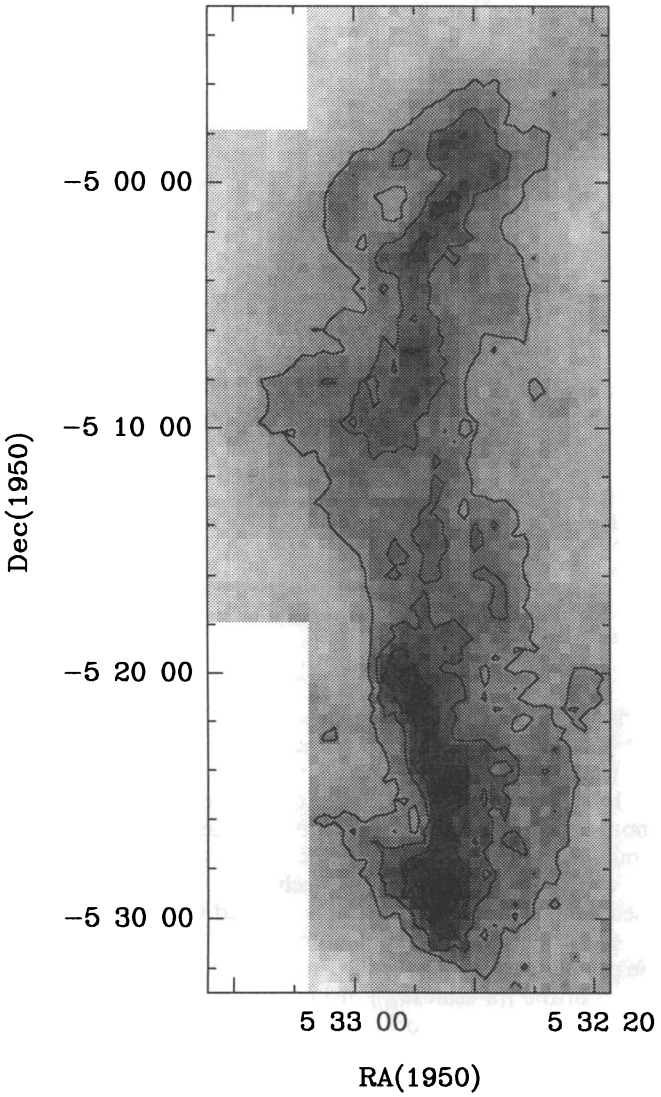

FIG. 5.—^{13}CO(1–0) contour map of integrated intensity in Orion A-North. The spectra have been integrated over 5–14 km s^{-1}. The peak contour flux is 31 K km s^{-1}; the contour interval is 5 K km s^{-1} and ranges from 10 to 25 K km s^{-1}. The gray scale ranges from −5 to 31 K km s^{-1} in equal steps of 1 K km s^{-1}. The southern ^{13}CO condensation contains the BN-KL nebula, which we excluded from our analysis together with all nearby cores, whose physical properties may have been strongly affected by the high dynamical activity in this region.

The mean line width $\langle \Delta v \rangle$ has been corrected for spectrum resolution, Δv_{res}, using the expression:

$$\langle \Delta v \rangle_{cor} = [(\langle \Delta v \rangle)^2 - (\langle \Delta v_{res} \rangle)^2]^{1/2} , \quad (5)$$

where $\Delta v_{res} = 0.69$ km s^{-1}. We adopted the values of line widths calculated from equation (5).

In NGC 2071 North, each C^{18}O spectral line observed at the Haystack antenna (see § 2.2.1) has been analyzed using the Continuum and Line Analysis Single-Dish Software (CLASS), installed at the Haystack Observatory. We derived line widths, Δv_i, relative to each spectrum using the second moment of the velocity profiles (eq. [1]) multiplied by $(8 \ln 2)^{1/2}$; then we calculated the mean line width and the associated standard deviation. The method is equivalent to that used for the FCRAO data. The results are listed in column (9) of Table 1. The table reports, for each cloud, the telescope used and the observed molecule in columns (2) and (3), respectively; position of the peak in the integrated intensity map in columns (4) and (5); columns (6)–(8) contain integrated intensity, mean velocity calculated from equation (2), and line width of the spectrum at the peak position, respectively. The relatively low value of integrated intensity for the C^{18}O spectrum in NGC 2071 North reflects the lower beam efficiency of the Haystack antenna in comparison with the FCRAO (see § 2.2). Columns (9)–(11) list parameters relative to the HM contour: Δv_1, the mean line width (see above); Δv_2, the line width of the mean spectrum (see § 3.1.2); R, the radius of the cloud (see § 3.2).

3.1.2. *Line Width of the Mean Spectrum*

We computed the line width relative to each cloud mapped at the FCRAO antenna using another method: all the spectra contained inside the half-maximum contour have been averaged together, to obtain the mean spectrum; then we calculated the line width of the mean spectrum following the second moment analysis described in the previous section. Similarly, the C^{18}O spectra obtained at the Haystack antenna toward NGC 2071 North have been averaged together to obtain the mean spectrum and the corresponding line width. The results (Δv_2) are listed in column (10) of Table 1. The uncertainties in the measured values of the line width of the mean spectrum have been estimated applying the error propagation formula to equation (1). The variables affected by error in equation (1) are $T^*_{Aki}(\alpha, \delta)$, whose uncertainty is given by the rms of the noise of the spectrum (ΔT_{rms}). Eliminating the subscripts i and j from equation (1), and propagating the errors, the uncertainty on σ_v

TABLE 1

LINE WIDTHS AND SIZES OF ORION CLOUDS OBSERVED AT THE FCRAO AND HAYSTACK ANTENNAS

			MAP PEAK					HM CONTOUR		
REGION	TELESCOPE	MOLECULE	R.A. (1950)	Decl. (1950)	$\int T^*_A dv$ (K km s^{-1})	V_{LSR} (km s^{-1})	Δv_{obs}	Δv_1	Δv_2[a]	R
NGC 2071 North.....	FCRAO	^{13}CO	05^{h}45^{m}06^s.9	00°41′14″.4	10.5	9.21	2.31	1.34 ± 0.03	1.37 ± 0.02	7.06
NGC 2071 North.....	Haystack	C^{18}O	05 45 06.9	00 39 11.0	0.7	9.12	1.18	1.13 ± 0.05	1.22 ± 0.01	4.98[b]
NGC 2071.....	FCRAO	^{13}CO	05 44 18.4	00 21 59.3	16.6	9.36	2.31	1.72 ± 0.02	2.16 ± 0.02	9.01
NGC 2068.....	FCRAO	^{13}CO	05 44 13.3	00 08 35.8	16.8	10.20	1.98	1.46 ± 0.02	1.67 ± 0.01	7.45
Ori B9	FCRAO	^{13}CO	05 39 58.3	−01 21 55.1	8.7	9.12	1.83	1.27 ± 0.05	1.41 ± 0.03	4.92
Ori B9	FCRAO	C^{18}O	05 39 58.3	−01 21 57.7	2.4	9.10	1.16	0.69 ± 0.07	0.96 ± 0.08	2.04
Orion A North	FCRAO	^{13}CO	05 32 43.3	−05 00 57.6	22.1	10.77	2.14	1.67 ± 0.03	2.00 ± 0.02	5.31

[a] Δv_1 and Δv_2 are the mean line width and the line width of the mean spectrum, respectively (see § 3).
[b] The size of the C^{18}O half maximum contour map in NGC 2071 North is from Iwata, Fukui, & Ogawa 1988.

($\sigma_{\sigma v}$) is given by

$$\sigma_{\sigma v} = \frac{\Delta T_{\rm rms}}{2\sigma_v N \langle T_A^* \rangle} \{\sum_{k=1}^{N} [(v_k - \langle v \rangle)^2 - \sigma_v^2]^2\}^{1/2} , \quad (6)$$

where $\langle T_A^* \rangle = (\sum_{k=1}^{N} T_{Ak}^*)/N$ is the mean antenna temperature of the line, and N is the total number of channels over which the spectra have been integrated.

From Table 1 we note that Δv_2 is always bigger than Δv_1, with the only exception being NGC 2071 North. This general tendency may reflect the existence of velocity gradients across the clouds; in this case the mean spectrum will result broader than individual spectra because it is the result of the sum of spectra at different mean velocities. In this work, we adopted the line width values calculated with the first method (i.e., the mean line width, Δv_i), which is more frequently used in the literature.

Table 1 shows how much the dispersion in the centroid velocity affects the evaluation of line widths at the size scale of $C^{18}O$ and ^{13}CO clouds, but data are not available to allow the same analysis for the smaller NH_3 cores. We estimate this effect by analyzing ammonia observations in the S140/L1204 molecular cloud made by Ungerechts, Walmsley, & Winnewisser (1986, hereafter UWW). UWW list intrinsic NH_3 line widths and LSR velocities at each observed position of the S140 map. We grouped the observed positions of their map in crossed grids of five spectra, and we calculated the dispersion in the centroid velocity in each group of spectra. This dispersion is a good measure of the change in the centroid velocity across the beam at the center of the grid. Comparing this dispersion with the dispersion of the mean profile in each group, we found that the dispersion in centroid velocity is only 7%–22% of the intrinsic NH_3 line width. Since this dispersion in centroid velocity adds in quadrature to the profile dispersion to give dispersion of the larger scale profile, the likely increase in width is at most a few percent. If this result can be extrapolated to massive ammonia cores in general, we could conclude that the dispersion in the centroid velocity gives no significant contribution on line width, at the size scales of ammonia cores.

3.2. *Size Estimates*

The radius of each cloud "i" (R_i) has been calculated from the area A_i inside the HM contour divided by π [$R_i = (A_i/\pi)^{1/2}$]. The choice of the half-maximum contour for calculating the size of each cloud has been made to have a unique definition applicable to every cloud in our massive cores sample, which contains our data as well as data from the literature (see § 3.3). The results are listed in column (11) of Table 1. Linear sizes of the whole sample have been calculated assuming a distance of 400 pc for Orion B (LBS) and 450 pc for Orion A (TUKH). We did not map NGC 2071 North in $C^{18}O$, therefore the size of this cloud has been adopted from IFO, where the authors give the linear size of the major and minor axes of the cloud; in Table 1 we report half of the arithmetic mean of the two axes, after correcting for the distance from the cloud adopted by IFO (= 500 pc). The choice of the arithmetic mean of the two cloud axes, instead of the geometric mean used in previous works (e.g., MF), has been made to have consistency with literature data (see § 3.3).

In the case of Orion A North, whose ^{13}CO contour map is shown in Figure 5, we identify two main molecular condensations: one in the north, containing four ammonia cores mapped by CW and the Orion Molecular Cloud 2 (OMC 2); the other condensation (southern part of the map) peaks in integrated intensity at the position of the BN-KL nebula. The HM contour relative to the northern condensation ($\int T_A^* dv = 11.1$ K km s^{-1}), extends over all the mapped region, including also the southern condensation. However, considering the integrated intensity variation along the map for a fixed value of right ascension, and looking at the gray-scale map, we note a depression in integrated intensity at a declination of about $-5°12'$. This valley in the integrated intensity map may be explained considering two blended clouds. From the integrated intensity profiles along the cloud we conclude that the northern ^{13}CO cloud in Orion A North (Fig. 5) reaches the HM level toward south at $\delta_c(1950) \sim -5°13'$. We therefore cut the map at this value of declination and included in the computation of the Orion A North size the area north of δ_c and limited by the HM contour. The uncertainty in the position of the cut does not significantly affect the estimate of the cloud size; for example, considering an error of 1′ in δ_c ($\delta_c' = \delta_c \pm 1'$), the corresponding uncertainty in the computation of R is $\sim$ 0.25, or $\sim$5% of the estimated value, which is negligible for the purpose of this work.

3.3. *The Massive Core Sample*

From the literature search and our observations we found 24 cores with at least three maps in different molecular lines and good estimates of line widths and sizes. The sample of massive cores is reported in Tables 2A and 2B. Columns (3)–(5) of Table 2A give positions and velocities ($V_{\rm LSR}$) of each core, in order of declination, based on ammonia observations; column (6) reports names of known clouds in which the cores are embedded or known stellar objects associated with the core. In Table 2B line widths and sizes of cores in every molecular line tracers are listed; in column (2) there are core names; in column (3) the mapped molecules and the corresponding transitions are listed; linear sizes R relative to HM contour maps are in column (4); in column (5) we report the corresponding nonthermal components of the line widths ($\Delta v_{\rm NT}$) for the mean molecular mass $m = 2.33$ amu; references for each observational data are reported in column (6). For the calculation of $\Delta v_{\rm NT}$ we assumed a kinetic temperature as given by HWW or CW; otherwise we used $T_K = 18$ K (see § 4). For the CS cores observed by LBS we calculated the size at the HM contour starting from the radius at the 5 σ level and the peak intensity, given by LBS, and assuming for each core a Gaussian shape.

Our method in determining the size of a cloud (see § 3.2) differ from some of the methods used by other authors in the literature. In particular, TUKH reported the radius of each CS core as half of the arithmetic average of linear extents (FWHM in the peak intensity) on position-velocity ($P-V$) diagrams (for each core candidate, TUKH made four $P-V$ diagrams passing through the CS(1–0) peak position); the value obtained has then been corrected for broadening due to the telescope beam. Other authors (Pastor et al. 1991; Anglada et al. 1989; SFOK) give the major and minor axis of the FWHM map and we calculated the arithmetic mean in analogy with TUKH. If we apply this method to our maps we find values of radii R' which do not differentiate by more than 10% the R values listed in Table 2B, the only exception being NGC 2068 where $R' = 1.14\ R$; this discrepancy is mostly due to the irregular shape of the region (see Fig. 1) in comparison with the other clouds mapped in this work (see Figs. 1, 3, and 5) where the greatest shape irregularities are limited to small boundary

TABLE 2

A. MASSIVE CORE POSITIONS AND VELOCITIES[a]

Number	Name	R.A. (1950)	Decl. (1950)	V_{LSR} (km s^{-1})	ID[b]	Reference
1	Ori B1	05^{h}44^{m}59^s.9	00°40′40″	9.3	NGC 2071 North	1
2	Ori B2	05 44 54.6	00 39 20	9.4	NGC 2071 North	1
3	Ori B3	05 45 02.6	00 38 40	9.7	NGC 2071 North	1
4	Ori B4	05 45 10.6	00 37 20	9.2	NGC 2071 North	1
5	Ori B5	05 44 52.5	00 19 48	9.3	NGC 2071	2
6	Ori B6	05 45 03.2	00 19 08	9.2	NGC 2071	2
7	Ori B7	05 43 33.8	−00 10 48	10.2	NGC 2068	2
8	Ori B8	05 43 33.8	−00 14 48	10.4	NGC 2068	2
9	Ori B9	05 39 55.5	−01 21 24	9.1	...	2
10	Ori A1	05 33 01.0	−05 00 42	11.9	ON 1	3
11	Ori A2	05 32 50.3	−05 02 42	11.1	ON 2	3
12	Ori A3	05 32 58.3	−05 05 22	11.2	ON 3	3
13	Ori A4	05 32 57.0	−05 09 22	11.7	ON 5	3
14	Ori A5	05 32 58.6	−05 11 42	11.2	OMC 2	4
15	Ori A6	05 32 45.3	−05 29 07	9.2	...	2
16	Ori A7	05 32 41.6	−05 38 00	8.3	OS 4/5	3
17	Ori A8	05 32 29.6	−05 48 00	7.6	OS 6	3
18	Ori A9	05 33 52.7	−06 24 02	7.1	L1641-North	2
19	Ori A10	05 33 03.7	−06 28 53	8.7	HH 34	5
20	Ori A11[c]	05 33 48.8	−06 50 23	8.4	HH 1-2	6
21	Ori A12	05 36 20.9	−07 02 43	3.3	L1641-Center	2
22	Ori A13	05 36 18.2	−07 02 43	4.7	...	2
23	Ori A14	05 36 55.1	−07 27 54	4.6	H 4-255	2
24	Ori A15	05 37 31.6	−07 31 19	4.8	L1641-S3	2

NOTE.—Cores have been listed in order of declination.

[a] Positions and velocities refer to NH_3 data.

[b] ID shows if the core is contained in a known cloud or associated with a known stellar object.

[c] For Ori A11 we use CS data because no ammonia observations have been published.

REFERENCES.—(1) Iwata, Fukui, & Ogawa 1988; (2) Harju, Walmsley, & Wouterloot 1993; (3) Cesaroni & Wilson 1994; (4) Bartla et al. 1983; (5) Anglada et al. 1989; (6) Tatematsu et al. 1993.

areas which do not significantly affect the final value of the cloud size.

Each core in Table 2 has been mapped in at least two small-size-scale molecular tracers, basically NH_3 and CS, and in ^{13}CO. The only exception is Ori A14 whose ^{13}CO line widths and sizes have not been measured; we included this object in our list because it has three well-resolved maps. However, the line width–size relation of Ori A14 will not be individually significant because of the lack of information at scales larger than a few tenths of a parsec.

4. THE LINE WIDTH–SIZE RELATION

All the data listed in Table 2B have been used to find the line width–map size relation in massive cores. In Figure 6*a* the nonthermal component of the line width is plotted versus the corresponding size for the cores in Table 2B. Different symbols represent different molecules. The dashed horizontal line is the estimated thermal part of the line width of the molecule of mean mass, calculated assuming a kinetic temperature $T_K = 18$ K, typical of massive cores. In fact, the average kinetic temperature in the HWW sample of ammonia cores in Orion is 16 ± 5, whereas the average T_K for ammonia cores in Orion A mapped by CW is 18 ± 2 K; finally, considering the ammonia cores in our sample (see § 3.3) where estimates of kinetic temperature are available, and averaging the values we find $T_K \sim 18$ K. Then we assume $T_K = 18$ K as the average value of kinetic temperature in Orion massive cores. The best-fit straight line for the data in Figure 6*a* is

$$\log \Delta v_{NT}(\mathrm{km\ s^{-1}}) = (0.23 \pm 0.03) + (0.21 \pm 0.03) \log R(\mathrm{pc}) \quad \mathscr{R} = 0.56 , \quad (7)$$

where $\mathscr{R}$ is the linear correlation coefficient.

In Figure 6*b* the Δv_{NT}–R relation for eight low-mass cores in Perseus, Taurus, Orion, Ophiuchus, and Cepheus mapped in NH_3, CS, and $C^{18}O$ (FM) is reported. To the data presented by FM we added new ^{13}CO observations (Fukui & Mizuno 1992), marked by diamonds in Figure 6*b*. The inclusion of ^{13}CO data furnished larger scale information, and increased the range of observational data to a size comparable with that relative to massive cores ($0.03 \leq R \leq 1$ pc). For consistency with the massive core sample, in Figure 6*b* we did not include the other six cores studied by FM for which ^{13}CO data are not available. The dashed thermal line has been calculated assuming $T_K = 10$ K, typical temperature of low-mass cores (Benson & Myers 1989). The new line width–size relation in low-mass cores has a slightly smaller slope than found by FM:

$$\log \Delta v_{NT}(\mathrm{km\ s^{-1}}) = (0.18 \pm 0.06) + (0.53 \pm 0.07) \log R(\mathrm{pc}) \quad \mathscr{R} = 0.81 . \quad (8)$$

Comparing Figure 6*a* with Figure 6*b* it is evident that the slope of the line width–size relation in massive cores is shallower than in low-mass cores; another clear difference is the radius at which the best-fit to the data in Figure 6 crosses the thermal line, which we call r_{TNT} (see § 5). In massive cores, r_{TNT} is ~ 15 times smaller than in low-mass cores. This implies that in massive cores nonthermal motions dominate over thermal ones at all observed size scales and probably at smaller ones, whereas in low-mass cores nonthermal motions become evident in all lines whose emission is extended over more than ~ 0.1 pc. Looking at Figure 6 we can see that ammonia cores (open circles) play a crucial role in determining the difference between massive and low-mass cores.

In Figures 7 and 8 the line width–size relation in individual massive and low-mass cores, respectively, is shown. To make a

TABLE 2—*Continued*

B. MASSIVE CORE LINE WIDTHS AND SIZES

Number	Name	Molecule	R (pc)	Δv_{NT} (km s^{-1})	Reference
1	Ori B1	^{13}CO (1 → 0)	0.82	1.33	1
		C^{18}O (1 → 0)	0.58	1.13	1, 2
		CS (2 → 1)	0.40	1.70	2, 3
		NH_3 (1, 1)	0.04	0.67	2
2	Ori B2	^{13}CO (1 → 0)	0.82	1.33	1
		C^{18}O (1 → 0)	0.58	1.13	1, 2
		CS (2 → 1)	0.40	1.70	2. 3
		NH_3 (1, 1)	0.08	1.18	2
3	Ori B3	^{13}CO (1 → 0)	0.82	1.33	1
		C^{18}O (1 → 0)	0.58	1.13	1, 2
		CS (2 → 1)	0.40	1.70	2, 3
		NH_3 (1, 1)	0.09	1.08	2
		HCO^+ (1 → 0)	0.14	1.09	2, 3
4	Ori B4	^{13}CO (1 → 0)	0.82	1.33	1
		C^{18}O (1 → 0)	0.58	1.13	1, 2
		CS (2 → 1)	0.40	1.70	2, 3
		NH_3 (1, 1)	0.12	0.77	2
5	Ori B5	^{13}CO (1 → 0)	1.05	1.71	1
		CS (2 → 1)	0.09	2.12	5
		NH_3 (1, 1)	0.04	0.98	6
6	Ori B6	^{13}CO (1 → 0)	1.05	1.71	1
		CS (2 → 1)	0.21	1.46	5
		NH_3 (1, 1)	0.10	0.77	6
7	Ori B7	^{13}CO (1 → 0)	0.87	1.45	1
		CS (1 → 0)	0.61	1.60	4
		CS (2 → 1)	0.45	1.43	5
		NH_3 (1, 1)	0.09	0.67	6
8	Ori B8	^{13}CO (1 → 0)	0.87	1.45	1
		CS (1 → 0)	0.61	1.60	4
		CS (2 → 1)	0.45	1.43	5
		NH_3 (1, 1)	0.09	0.57	6
9	Ori B9	^{13}CO (1 → 0)	0.57	1.26	1
		C^{18}O (1 → 0)	0.24	0.67	1
		CS (2 → 1)	0.21	1.39	5
		NH_3 (1, 1)	0.07	0.57	6
10	Ori A1	^{13}CO (1 → 0)	0.70	1.66	1
		CS (1 → 0)	0.14	1.00	7
		NH_3 (1, 1)	0.09	1.18	8
11	Ori A2	^{13}CO (1 → 0)	0.70	1.66	1
		CS (1 → 0)	0.23	1.74	7
		NH_3 (1, 1)	0.10	0.87	8
12	Ori A3	^{13}CO (1 → 0)	0.70	1.66	1
		CS (1 → 0)	0.14	0.81	7
		NH_3 (1, 1)	0.09	0.77	8
13	Ori A4	^{13}CO (1 → 0)	0.70	1.66	1
		CS (1 → 0)	0.20	1.92	7
		NH_3 (1, 1)	0.10	0.87	8
14	Ori A5	^{13}CO (1 → 0)	0.70	1.66	1
		CS (1 → 0)	0.18	1.32	7
		NH_3 (1, 1)	0.04	0.97	9
15	Ori A6	^{13}CO (1 → 0)	0.50	1.98	10
		CS (1 → 0)	0.11	0.97	7
		NH_3 (1, 1)	0.08	1.47	6
16	Ori A7	^{13}CO (1 → 0)	0.45	1.19	10
		CS (1 → 0)	0.29	0.87	7
		NH_3 (1, 1)	0.12	0.87	8
17	Ori A8	^{13}CO (1 → 0)	0.59	2.79	11
		CS (1 → 0)	0.27	1.18	7
		NH_3 (1, 1)	0.09	1.38	8
18	Ori A9	^{13}CO (1 → 0)	0.85	2.69	11
		CS (1 → 0)	0.22	1.75	7
		NH_3 (1, 1)	0.09	0.98	6
		HCO^+ (1 → 0)	0.08	1.93	12
		HCN (1 → 0)	0.10	0.99	13
19	Ori A10	^{13}CO (1 → 0)	0.33	1.29	11
		CS (1 → 0)	0.15	1.00	8
		NH_3 (1, 1)	0.20	0.73	14
20	Ori A11	^{13}CO (1 → 0)	0.63	2.89	11
		CS (1 → 0)	0.23	1.74	7
		CS (2 → 1)	0.35	1.25	15
21	Ori A12	^{13}CO (1 → 0)	0.68	1.69	11
		CS (1 → 0)	0.16	1.48	7
		NH_3 (1, 1)	0.04	0.88	6
		HCO^+ (1 → 0)	0.04	0.95	12
22	Ori A13	^{13}CO (1 → 0)	0.68	1.69	11
		CS (1 → 0)	0.16	1.48	7
		NH_3 (1, 1)	0.05	0.66	6
23	Ori A14	CS (1 → 0)	0.27	1.37	7
		NH_3 (1, 1)	0.05	0.88	6
		HCO^+ (1 → 0)	0.05	2.20	12
24	Ori A15	^{13}CO (1 → 0)	0.75	2.39	11
		CS (1 → 0)	0.23	1.15	7
		NH_3 (1, 1)	0.17	1.09	6

REFERENCES.—(1) This work; (2) Iwata, Fukui, & Ogawa 1988; (3) Goldsmith et al. 1992; (4) Pastor et al. 1991; (5) Lada, Bally, & Stark 1991; (6) Harju, Walmsley, & Wouterloot 1993; (7) Tatematsu et al. 1993; (8) Cesaroni & Wilson 1994; (9) Bartla et al. 1983; (10) Sugitani et al. 1987; (11) Bally et al. 1987; (12) Chen, Fukui, & Yang 1992; (13) Fukui et al. 1988; (14) Anglada et al. 1989; (15) Heyer et al. 1986.

more consistent comparison, only those cores where at least NH_3, CS, and ^{13}CO are available have been considered. From the massive core sample we therefore excluded Ori A11, and Ori A14. We also excluded HCO^+ data which is available for only three of the remaining 22 cores. This line generally shows line widths significantly broader than ammonia lines (e.g., in Ori A9), suggesting that this species is probably tracing more turbulent gas than the (1, 1) inversion transition of ammonia.

In Figure 7, those cores differing from each other only in ammonia data (i.e., where multiple ammonia cores are embedded in the same CS and ^{13}CO HM contours) have been plotted in the same diagram (see Ori B1–4, and Ori B7–8). Different thermal (dashed) lines in Figure 7 reflect the different observed values of kinetic temperatures. If temperature values were not available from literature, we assumed $T_k = 18$ K, as already discussed. The intercept b and slope q of individual best fits to the data in Figures 7 and 8 are listed in Table 3 (cols. [2] and [3], respectively), together with the associated errors. The errors are generally large because of the small amount of data in each core. The temperature of ammonia cores are listed in column (4). Column (5) reports r_{TNT}, the radius at which the thermal and nonthermal component of the line width are equal. In columns (6) and (7) there are two parameters of the TNT model which will be discussed in the next section. In column 8 the column density of the TNT cloud along a line of sight 0.1 pc away from the cloud center is reported (see § 5.1.2).

Comparing Figure 7 with Figure 8, and looking at Table 3, we note that massive cores generally tend to have shallower

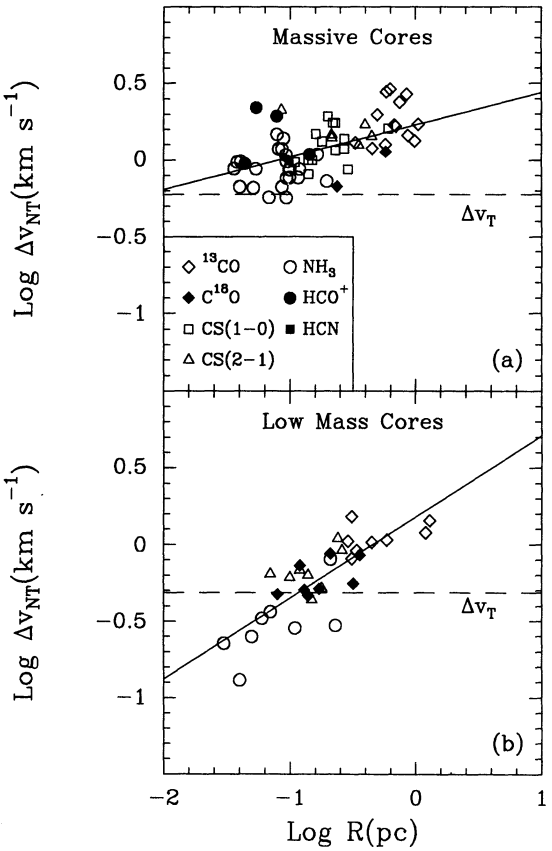

FIG. 6.—Line width–size relation in (*a*) *massive* cores in Orion, and (*b*) *low-mass* cores in Perseus, Taurus, Orion, Ophiuchus, and Cepheus. Dashed lines labeled Δv_T represent the thermal part of the line width of the molecule of mean mass, assuming temperature 18 K (massive cores), or 10 K (low-mass cores). The positions of ammonia cores in these Δv–R diagrams play a crucial role in determining differences between massive and low-mass cores (see text).

slopes than low-mass cores, in agreement with the general relations shown in Figures 6*a* and 6*b*. In particular, assuming a Gaussian distribution of the errors in b and q (see Table 3), we calculated the mean values ($\langle b \rangle$, and $\langle q \rangle$), and associated errors ($\sigma_{\langle b \rangle}$, and $\sigma_{\langle q \rangle}$) of these two prarameters, both for massive and low-mass cores. We point out that these results will reflect an average property of individual cores, therefore it allows to verify if the line width increases with map size from line to line within single cores. From the calculation of $\langle b \rangle$ and $\langle q \rangle$ of low-mass cores, we eliminated L1535 and L255 because of their peculiar steep slopes. These two objects cannot be modeled as TNT spheres as we will see in § 5.1.1. The results are shown by the following relations:

$$\log \Delta v_{NT}(\mathrm{km\ s^{-1}}) = (\langle b \rangle \pm \sigma_{\langle b \rangle}) + (\langle q \rangle \pm \sigma_{\langle q \rangle}) \log R(\mathrm{pc}) ,$$

$$= (0.26 \pm 0.01) + (0.21 \pm 0.01) \log R(\mathrm{pc}) ,$$

for massive cores

$$= (0.11 \pm 0.04) + (0.51 \pm 0.06) \log R(\mathrm{pc}) ,$$

for low-mass cores

The above numbers are identical, within the errors, to those reported in equations (7) and (8), for massive and low-mass cores, respectively. This proves that the general line width–size relation is mainly due to the variation of line width with size within the cores in the sample rather than to any core-to-core variation, as indicated by FM.

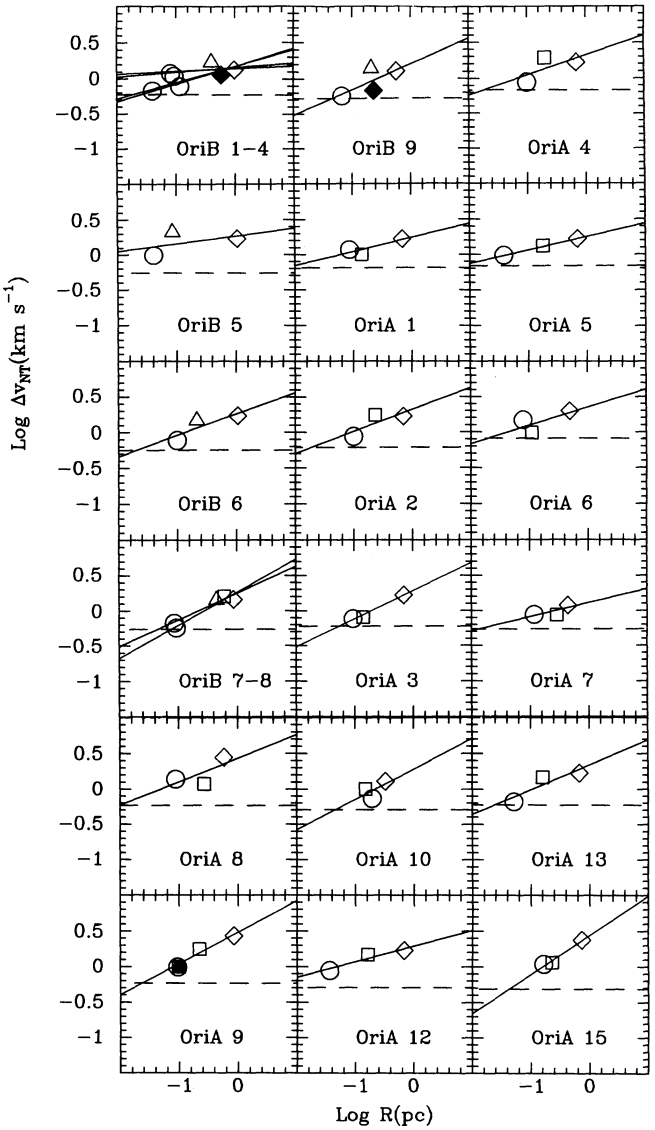

FIG. 7.—Line width–size relation for indvidual massive cores in Table 2. Best fits are listed in Table 3. Symbols are the same as in Fig. 6. Dashed lines define the thermal line width for each core, accounting for the relative kinetic temperature. Multiple ammonia cores embedded in the same ^{13}CO, and CS cloud have been included in the same diagram, as in the case of Ori B1–4, and Ori B7–8.

5. "TNT" MODELS OF MASSIVE AND LOW-MASS CORES

5.1. *Hydrostatic Equilibrium Models*

5.1.1. *Velocity Dispersion and Density*

The model which includes thermal and nonthermal motions (TNT) in a spherically symmetric system in hydrostatic equilibrium (HSE) has been introduced by Myers & Fuller (1992). The thermal velocity disperion σ_T inside the spherically symmetric core is spatially uniform, whereas the nonthermal component σ_{NT} increases with radius r as a power-law, as indicated by observations. The total one-dimensional velocity dispersion σ is given by adding in quadrature the two components:

$$\sigma^2 = \sigma_T^2 + \sigma_{NT}^2 . \qquad (9)$$

The radius at which σ_T and σ_{NT} are equal is called r_{TNT}. For $r \ll r_{TNT}$ the TNT core reduces to the singular isothermal

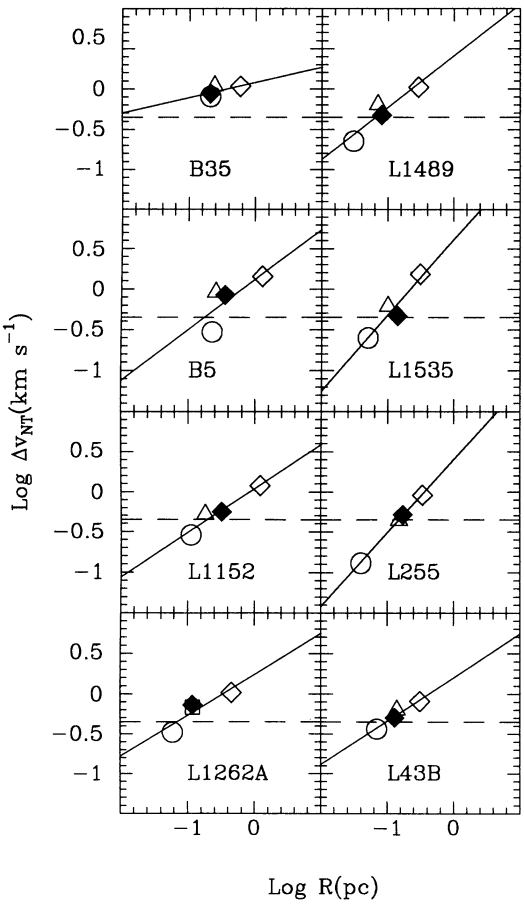

FIG. 8.—Line width–size relation for individual low-mass cores. Symbols are as in Fig. 7. Best fits to the data are reported in Table 3. The slope in the individual line width–size relation is generally steeper than in massive cores (see Fig. 7), as in the general relation shown in Fig. 6.

sphere (SIS; Shu 1977) where the dependence of density on radius r goes like r^{-2}; at $r \geq r_{TNT}$ MF found that the core density and pressure in the TNT model are larger by a significant factor and have shallower gradients than do SIS values, leading to a better agreement with observations. MF applied the TNT model to the core in L1204 associated with the H II region S140, and found that the nonthermal component of the line width in L1204 follows the trend $\Delta v_{NT} \sim R^q$ where $q = 0.5 \pm 0.1$. This value of q is significantly different from what we found in Orion, where $q \sim 0.2$ (see eq. [7]); therefore we consider here a more general version of the MF model, not restricted to $q = \frac{1}{2}$, and apply this model to the new line width–size relations in massive and low-mass cores (see § 4).

The basic assumption of spherically symmetric clouds is not correct, because of the observational evidence that many cores and clouds have axial ratio $a = 0.4$–0.5 (Myers et al. 1991). However, our main purpose is to estimate how inclusion of the observed nonthermal motions changes the density structure from that of a spherical, isothermal cloud. Furthermore, aspherical clouds have been studied in detail by Bertoldi & McKee (1992) during their analysis of pressure-confined clumps in magnetized molecular clouds. Their expression (A9) gives the gravitational energy of an ellipsoidal cloud with a power-law density distribution. Using this expression we can calculate the gravitational energy ratio (g) between a spherical cloud of radius R and an ellipsoidal cloud with the same density distribution and geometric mean radius. The semimajor axis is then $R/a^{1/2}$, and the semiminor axis is $R\,a^{1/2}$. We obtain $g = 0.59$ and $g = 0.44$ when the axial ratio a is 0.5 and 0.3, respectively. The average density of the cloud, proportional to the square root of the gravitational energy, decreases from the spherical case by $\sim 10\%$, and is then only weakly dependent on the cloud shape. Therefore, our use of spherical models is sufficient to estimate density structure in moderately aspheroidal clumps and clouds.

We start from the equation of HSE (Chandrasekhar 1939; MF). If $\sigma_{NT}(r)$ increases approximately as r^q, and σ_T is spatially uniform, the equation of HSE can be solved for a density law of the form:

$$n(r) = \frac{\sigma_T^2}{2\pi m G r_0^2}\,(x^{-2} + x^{-p})\,, \tag{10}$$

where p is an adjustable parameter, approximately equal to $2 - 2q$ for a certain range of q (see MF); $x = r/r_0$, and r_0 is the radius where the density components which vary as r^{-p} and r^{-2} are equal; m is the mass of the molecule of mean mass, and G is the gravitational constant. If nonthermal motions vanish, equation (10) reduces to the density law for a single isothermal sphere.

Substituting equation (10) and the expression of the kinetic pressure P at r,

$$P(r) = mn(r)[\sigma_T^2 + \sigma_{NT}^2(r)]\,, \tag{11}$$

in the equation of HSE, we obtain the general expression for the velocity dispersion in the HSE model:

$$\sigma_{NT}^2(x) = \sigma_T^2\left(\frac{8 - 5p + p^2}{p(3-p)}\,x^{-p} - \frac{x^{2-2p}}{(3-p)(1-p)} + C\right) \times \frac{1}{(x^{-2} + x^{-p})}\,, \tag{12}$$

where C is independent of r:

$$C = \left(\frac{\sigma_{max}}{\sigma_T}\right)^2 x_{max}^{-2} + \left[\frac{-8 + 5p - p^2}{p(3-p)} + \left(\frac{\sigma_{max}}{\sigma_T}\right)^2\right] x_{max}^{-p} + \frac{x_{max}^{(2-2p)}}{(3-p)(1-p)}\,. \tag{13}$$

In equation (13) $\sigma_{max} \equiv \sigma_{NT}(r_{max})$, and $x_{max} \equiv r_{max}/r_0$, with r_{max} greater than or equal to r; $p > 0$, and $p \neq 1, 3$. The cases $p = 0$ and $p = 1$ are particular cases which must be solved by introducing the specific value of p in equation (10). MF considered the case $p = 1$. The assumed value of r_{max} is 10 pc and the corresponding σ_{max}, value of σ_{NT} at r_{max}, is given by substituting r_{max} in the empirical Δv_{NT}–R relation, solving for Δv_{NT}, and then dividing by $(8 \ln 2)^{1/2}$. If σ_{max} is calculated with the above method, r_{max} in the model can assume any value; in particular we could limit the calculation to $r_{max} = 1$ pc, the upper limit in the observed size range. In this case, the properties of the cloud for $r < 1$ pc will result the same as if we choose $r_{max} = 10$ pc. The model results which lie outside the observed range of size, must be regarded as a numerical extrapolation.

The relation between r_0 and r_{TNT} is obtained by setting $\sigma_{NT}(x_{TNT}) = \sigma_T$ in equation (12), where $x_{TNT} = r_{TNT}/r_0$. If we know, from the data, the slope and the intercept in the Δv_{NT}–R relation, and the value of r_{TNT}, we can vary r_0 and p until equation (12) reproduces the observed line width–size relation.

TABLE 3

LINE WIDTH–SIZE RELATION FOR INDIVIDUAL CORES

Core	b	q	T [K]	r_{TNT} [pc]	p	r_0 [pc]	N	σ_N^+	σ_N^-
							—[10^{21} cm^{-2}]—		
Massive Cores									
OriB 1	0.17±0.08	0.23±0.11	18	1.94×10^{-2}	1.6	2.84×10^{-2}	11	4	1
OriB 2	0.14±0.07	0.04±0.12	18	1.15×10^{-10}	1.9	8.70×10^{-10}	29	15	9
OriB 3	0.14±0.08	0.08±0.13	18	2.82×10^{-5}	1.8	3.42×10^{-5}	24	12	8
OriB 4	0.17±0.10	0.25±0.19	18	2.65×10^{-2}	1.5	4.29×10^{-2}	11	5	3
OriB 5	0.27±0.21	0.11±0.21	15	1.40×10^{-5}	1.8	1.71×10^{-5}	23	18	9
OriB 6	0.26±0.12	0.30±0.18	16	2.00×10^{-2}	1.4	3.59×10^{-2}	13	5	6
OriB 7	0.25±0.05	0.38±0.08	14	4.06×10^{-2}	1.3	8.26×10^{-2}	8	1	1
OriB 8	0.26±0.06	0.47±0.10	15	7.68×10^{-2}	1.2	1.88×10^{-1}	6	1	1
OriB 9	0.20±0.19	0.36±0.25	14	4.68×10^{-2}	1.3	9.47×10^{-2}	7	4	2
OriA 1	0.24±0.10	0.20±0.12	21	7.02×10^{-3}	1.6	1.03×10^{-2}	17	4	3
OriA 2	0.32±0.17	0.31±0.24	19	1.92×10^{-2}	1.4	3.44×10^{-2}	14	6	4
OriA 3	0.28±0.04	0.40±0.05	18	5.22×10^{-2}	1.3	1.13×10^{-1}	8.7	0.4	0.4
OriA 4	0.32±0.23	0.28±0.32	23	1.77×10^{-2}	1.5	2.85×10^{-2}	16	9	5
OriA 5	0.25±0.01	0.19±0.01	24	6.81×10^{-3}	1.6	9.97×10^{-3}	20	5	1
OriA 6	0.35±0.22	0.26±0.26	33	1.99×10^{-2}	1.5	3.21×10^{-2}	21	9	6
OriA 7	0.11±0.11	0.20±0.18	15	1.35×10^{-2}	1.6	1.98×10^{-2}	9	2	1
OriA 8	0.43±0.24	0.33±0.35	17	9.55×10^{-3}	1.4	1.72×10^{-2}	17	11	6
OriA 9	0.48±0.07	0.44±0.10	17	2.35×10^{-2}	1.2	5.60×10^{-2}	13	2	2
OriA 10	0.28±0.39	0.43±0.57	13	4.61×10^{-2}	1.2	1.08×10^{-1}	5	2	1
OriA 12	0.29±0.07	0.22±0.07	13	2.20×10^{-3}	1.55	3.37×10^{-3}	18	3	3
OriA 13	0.34±0.15	0.35±0.18	18	2.44×10^{-2}	1.3	4.94×10^{-2}	13	5	5
OriA 15	0.44±0.05	0.55±0.08	12	4.29×10^{-2}	1.15	1.31×10^{-1}	6	1	1
Low Mass Cores									
B35	0.08±0.10	0.19±0.17	10	5.34×10^{-3}	1.6	7.82×10^{-3}	8.7	1.9	1.4
B5	0.12±0.19	0.62±0.40	10	1.73×10^{-1}	1.0	8.13×10^{-1}	2.7	0.5	0.3
L1152	0.04±0.06	0.55±0.10	10	1.94×10^{-1}	1.1	6.19×10^{-1}	2.9	0.2	0.2
L1262A	0.24±0.16	0.51±0.17	10	6.91×10^{-2}	1.2	1.78×10^{-1}	3.7	0.7	0.5
L1489	0.41±0.19	0.64±0.17	10	6.45×10^{-2}	1.1	3.11×10^{-1}	2.6	0.3	0.4
L1535	0.61±0.23	0.93±0.23	10	...	...	...	...	...	...
L255	0.40±0.02	0.91±0.02	10	...	...	...	...	...	...
L43B	0.20±0.09	0.54±0.10	10	9.51×10^{-2}	1.1	3.03×10^{-1}	2.7	0.1	0.1

NOTES.—The massive core observational data are detailed in Tables 1, 2A, and 2B. The low-mass core data are detailed in Fuller & Myers 1992 and Fukui & Mizuno 1992. The column density N has been calculated at $b = 0.1$ pc (see § 5.1.2). The errors associated with the column density calculation [σ_N^+ and σ_N^-], reflect the dispersion in the Δv_{NT}-R relation and not the observational errors.

Once the values of r_0 and p giving best-fit to the line width–size relation are found, they are introduced in equation (10) to determine the density profile for a specific class of cores. The hydrostatic equilibrium model parameters for massive and low-mass cores are summarized in Table 4; the intercept b and the slope q in the log Δv_{NT}–log R relation are listed in columns (3) and (4), respectively; columns (5)–(7) report r_{TNT}, p, and r_0, respectively. Column (8) reports the column density N (see § 5.1.2). The same quantities are listed in columns 5 to 8 of Table 3 for individual cores.

The TNT model described by equations (9)–(13) was able to fit all the cores listed in Table 3, but in a small number of cases the best-fit model parameters are physically unrealistic. When the slope q of the line width–size relation is very shallow ($q < 0.15$, as for Ori B2, Ori B3, and Ori B5), the nonthermal component of the velocity dispersion resembles an isothermal gas at a temperature different from that of the thermal component (in the present case, hotter than the thermal component). Thus the values of r_0 and r_{TNT} are very small, and not well determined. When the slope is very steep ($q > 0.7$, as

TABLE 4

MODEL PARAMETERS FOR TYPICAL MASSIVE AND LOW-MASS CORES

Type of Core	Number of Cores	b[a]	q	r_{TNT} (pc)	p	r_0 (pc)	N[b] (10^{21} cm^{-2})
Massive	22	0.23 ± 0.03	0.21 ± 0.03	6.89×10^{-3}	1.6	1.01×10^{-2}	15^{+9}_{-5}
Low-Mass.....	8	0.18 ± 0.06	0.53 ± 0.07	9.92×10^{-2}	1.1	3.08×10^{-1}	$3.1^{+0.9}_{-0.5}$

[a] b and q are the intercept and the slope, respectively, in the log Δv_{NT}–log R relation (see eqs. [7] and [8]).
[b] The column density N has been calculated at a projected distance $b = 0.1$ pc from the center of the cloud (see § 5.1.2); the associated errors reflect the dispersion in the Δv_{NT}–R relation.

for L1535 and L255), the model can satisfy the equilibrium requirement of a negative pressure gradient only by forcing r_0 to exceed the range of observed map sizes. Then all the observed radii lie in the zone where the density is dominated by the thermal component, even though their corresponding line widths may be dominated by nonthermal motions, and the pressure gradient is negative, but nearly zero. This situation is probably unrealistic, because even a 10% uncertainty in the observed line width will allow the pressure gradient to be positive, violating the basic model assumption. Such solutions are formally correct, but not robust against a small variations in the data. We consider them unlikely to be realistic.

In Figure 9 we compare the density profiles in 24 massive and eight low-mass cores calculated starting from the line width–size relations in equation (7) and (8), respectively, and solving the equations of the TNT model. The dispersion in the calculation of the density profiles, represented by the lines marked $+1\sigma$ and -1σ, reflects the dispersion in the $\Delta v_{\rm NT}$–R relations, which has been calculated considering the general expression:

$$\sigma_y^2 = \frac{1}{N-1}\sum_{i=1}^{N}(y_i - b - qx_i)^2 ,$$

where σ_y represents the error associated with $y = \log \Delta v_{\rm NT}$(km s^{-1}), in the relation $y = b + qx$, where $x = \log R$(pc); N is the number of data points (x_i, y_i) in the $y - x$ relation. For values of R smaller than $\sim$0.3 pc and greater than $\sim$1 pc, indicated in Figure 9 by dashed lines, the model results are based on extrapolation beyond the range of observational data (see Fig. 6). The light density profiles indicate singular isothermal spheres at 10 and 18 K, respectively.

In Figure 9, massive and low-mass cores have significantly different density profiles. As we can see from Table 4, the nonthermal component of the density profile is steeper ($\propto r^{-1.6}$) in massive cores than in low-mass cores ($\propto r^{-1.1}$), and in the observational range the density is higher in massive cores by a factor of $\sim$5. Both TNT core models depart from the SIS result, especially in the massive case where the difference is evident also at small size scales; in effect all the cores in Table 2B have thermal velocity dispersions which are negligible if compared with the nonthermal part at size scales traced by NH_3 as well as by ^{13}CO. Figure 6*a* illustrate this phenomenon: almost all the ammonia data lie above the thermal line, and $r_{\rm TNT}$ is $\sim$6 times smaller than the radius of the smallest core in our sample. In Figure 9, low-mass cores are close to the 10 K SIS line until their size exceeds a few tenths of a parsec. Consequently all ammonia data in Figure 6*b* lie below the thermal line.

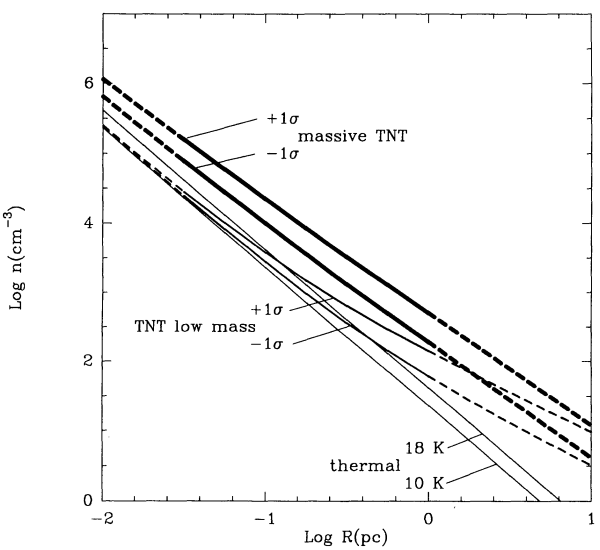

FIG. 9.—Density profiles in massive and low-mass cores obtained from the empirical Δv–R relation, and assuming a spherical symmetric cloud in hydrostatic equilibrium. The dispersion in the calculation of the density profiles (lines marked $\pm$ 1 σ) reflects the dispersion in the Δv–R relaion. The continuous lines trace the density profiles into the size range where the observational data are available (see Fig. 6). The thin lines refer to singular isothermal spheres at 10 and 18 K, where $n(r) \propto r^{-2}$. The nonthermal component of the density profile goes like $r^{-1.6}$ in massive cores and $r^{-1.1}$ in low-mass cores.

5.1.2. *Pressure, Mass, and Column Density*

The pressure in massive and low-mass cores, based on equation (11), is shown in Figure 10. At the size scales of ammonia cores ($r \leq 0.1$ pc) the pressure in massive cores is more than one order of magnitude bigger than in low-mass cores, and it remains significantly bigger inside the observed range of core sizes.

The mass interior to r is given by integrating equation (10) over radius:

$$M(<r) = \frac{2\sigma_T^2 r_0}{G}\left(x + \frac{x^{3-p}}{3-p}\right). \quad (14)$$

Using expression (14) we can calculate the average column density, defined by

$$\langle N\rangle_r = \frac{M(<r)}{\pi m r^2}. \quad (15)$$

Starting from the line width–size relations for massive and low-mass cores (eqs. [7] and [8], respectively), and using equation (15) we calculated the corresponding value of $\langle N\rangle_r$. Taking into account the dispersions in the two best fits shown in Figure 6, at $r = 0.1$ pc we find $\langle N\rangle_r = 1.4^{+0.7}_{-0.4} \times 10^{22}$ cm^{-2}

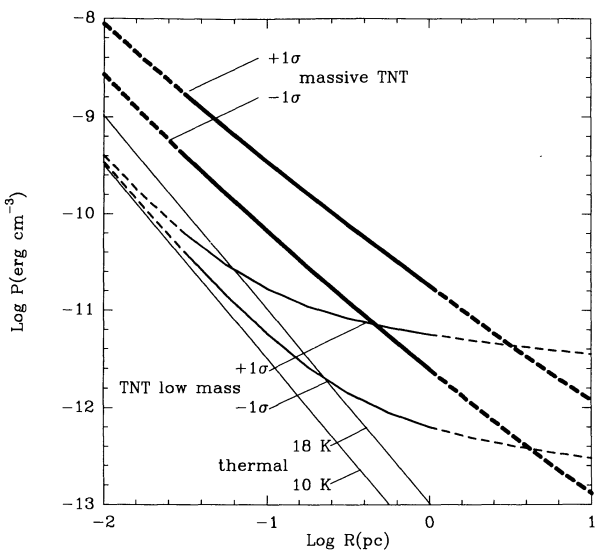

FIG. 10.—Pressure profiles for massive and low-mass cores in the TNT model. Symbols are the same as Fig. 9. Massive cores have a significantly greater pressure than low-mass cores, in particular at the size scales of ammonia cores ($r \sim 0.1$ pc).

for massive cores, while for low-mass cores $\langle N \rangle_r = 3.4^{+0.4}_{-0.2} \times 10^{21}$ cm^{-2}. In terms of visual extinction these values are $A_V = 15^{+8}_{-4}$, and $3.6^{+0.4}_{-0.3}$ mag, respectively.

These values of extinction appear consistent with representative observed values for low-mass and massive cloud cores, but an accurate comparison requires model estimates of the extinction at a given projected distance from the peak, rather than the mean extinction within a sphere. Therefore we calculated the visual extinction at a projected distance b from the center of the TNT cloud. If the projection of r along the line-of-sight is specified by z [$z = (r^2 - b^2)^{1/2}$], we obtain the column density at a projected distance b from the center of the cloud [$N(b)$] by integrating equation (10) along z:

$$N(b) = 2\int_0^{z_{max}} n(z)dz$$

$$= N_0\left[\frac{r_0}{b}\,\mathrm{arctg}\,\frac{z_{max}}{b} + r_0^{p-1}\int_0^{z_{max}} \frac{dz}{(b^2 + z^2)^{p/2}}\right]. \quad (16)$$

Here $N_0 \equiv \sigma_T^2/(\pi m G r_0)$ is the column density of the thermal component at $b = \pi r_0/2$, provided $b \ll z_{max}$. If $p = 1$ (the case studied by MF), we obtain

$$N(b) = N_0\left[\frac{r_0}{b}\,\mathrm{arctg}\,\frac{z_{max}}{b} + \ln\left(\frac{z_{max} + R_{max}}{b}\right)\right]. \quad (17)$$

If $p \neq 1$, expression (16) has been integrated numerically. Using equation (16) and limiting the integration at $z_{max} = (R_{max}^2 - b^2)^{1/2}$, where R_{max} is the average radius of the ^{13}CO half-maximum contour in the sample of massive and low-mass cores, we obtain, for $b = 0.1$ pc:

$$A_V^{TNT} = 16^{+9}_{-5} \text{ mag in 22 massive cores},$$

$$A_V^{TNT} = 3.3^{+0.9}_{-0.5} \text{ mag in 8 low mass cores}.$$

For low-mass cores, the value of visual extinction calculated with the TNT model (3.3 mag) is very close to the value found by Cenicharo & Bachiller (1984, hereafter CB) from star counts for 38 dark clouds in Taurus and Perseus at radius 0.1 pc ($A_V^* = 4.2 \pm 1.0$ mag). For massive cores, no systematic study like that of CB is available. However, in the well-studied massive core associated with IRAS 05338 − 0624 (Ori A9, no. 18 in Table 2A), infrared colors indicate that 19 embedded sources have A_V with mean ± standard deviation 20 ± 10 mag (Strom, Margulis, & Strom 1989). Thus the TNT model estimates of extinction (eq. [16]) are in good agreement with available observational estimates for similar objects, and also with the TNT model estimates of the mean extinction within a sphere (eq. [15]). In contrast, equation (16) indicates that infinite isothermal spheres at 18 and 10 K would have $A_V = 7.3$ and 2.2 mag, significantly lower than the corresponding observed and TNT model values.

It is also interesting to note that from star count studies, Cernicharo, Bachiller, & Duvert (1985) found a density structure of low-mass cores in Taurus and Perseus which follow the trend $n(r) \sim r^{-p}$, with $p = 1.3 \pm 0.2$. This result applies only for sizes larger than a few 0.1 pc, where nonthermal motions dominate, as we found in § 4. Therefore we can compare the density structure of the Taurus and Perseus complex of dark clouds, deduced from star counts, with the nonthermal component of the density profile of low-mass cores calculated with the TNT model. Our result is $p = 1.1$ (see Table 4), which coincides (within the errors) with that found by Cernicharo et al. (1985).

In the Appendix, we use the TNT model to predict the variation of line width with projected radius for a single density tracer. We show that a line width–size relation should also be observed by using a single species, although the slope is shallower than starting from different density tracers, especially for low-mass ammonia cores. We also show that the line width–size relation predicted by the TNT model is consistent with the observed line width–size relation used to fix the parameters of the model.

5.2. *Infall Models*

The above picture can be related to the infall properties of massive and low-mass cores. Following MF, we assume that the free fall of each radial layer of the TNT core is triggered by an "expansion wave" traveling outward at the local sound speed, as in the "inside-out" collapse of the SIS whose exact similarity solution was found by Shu (1977). Therefore, the time that all the mass within $r[M(<r)]$ takes to collapse to the origin, called the infall time t_{inf}, is the time t_{exp} for the expansion wave to reach r, plus the time t_{coll} for the gas at r to free fall to the origin: $t_{inf} = t_{exp} + t_{coll}$. MF used the term "accretion time" (t_{acc}) instead of "infall time." Here we use t_{inf} to avoid confusion with the accretion time, which is also used to indicate the accretion of a star through the circumstellar disk. The expression for t_{exp} is simply found by integrating $(r_0/\sigma)dx$ in between 0 and x, where σ is given in equation (9) (see eq. [16] in MF). A general expression for t_{col}, valid for every value of p, is

$$t_{coll}(r) = \frac{\pi r^{3/2}}{2[2GM(<r)]^{1/2}}, \quad (18)$$

where G is the gravitational constant, and $M(<r)$, the mass interior to r, is given by equation (14).

In Figure 11 the accreted mass M, given by equation (14), is plotted versus time from the start of infall, t_{inf}, for massive and

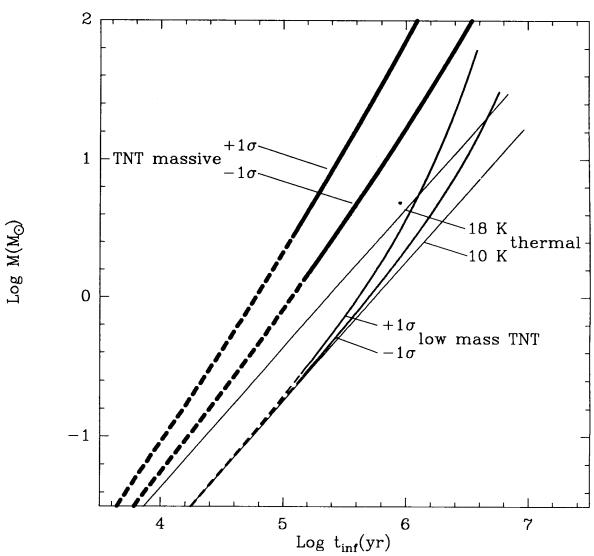

FIG. 11.—Accreted stellar mass M as a function of the infall time in massive and low-mass cores. Symbols as in Fig. 9. The lines become dashed to mark the values of the mass enclosed in a sphere of radius equal or less than "R_{min}," where R_{min} indicates the lowest value of the core radius available from observational data (shown in Fig. 6); therefore the dashed part of the diagram represents a numerical extrapolation to the observed physical properties in dense cores. The higher density and pressure in massive cores lead to values for t_{inf} ~6 times shorter than in low-mass cores.

low-mass cores. The change in the lines from continuous to dashed ones marks the values of the mass enclosed in a sphere of radius equal to "R_{min}," where R_{min} indicates the lowest value of the core radius available from the observational data shown in Figure 6. The higher density and pressure, and the smaller r_{TNT} in massive cores lead to values for $t_{inf} \sim 6$ times shorter than in low-mass cores. The time to accrete 1 $M_\odot$ is $\sim 7 \times 10^4$ yr for the massive case, value close to the star formation rate calculated by Hodapp & Deane (1993) for the small but dense cluster of young stars in L1641 North, one of the objects in our sample. In low-mass cores, the time to accrete 1 $M_\odot$ is $\sim 4 \times 10^5$ yr. From Figure 11 it is once again evident that the SIS model is not appropriate to describe massive cores; at $T_K = 18$ K the infall rate for a purely thermal core is $\sim 5 \times 10^{-6}\ M_\odot\ \mathrm{yr}^{-1}$, ~ 3 times smaller than using the TNT model. In contrast, the infall rate in low-mass cores almost coincides with a purely thermal core at 10 K, which is $2 \times 10^{-6}\ M_\odot\ \mathrm{yr}^{-1}$.

The higher infall rate found in massive cores is mostly due to their primarily nonthermal nature; also at the smallest size scale of the cores in the sample listed in Table 2B the nonthermal motions dominate. This shortens the infall time, compared with the mostly thermal low-mass cores, because the expansion wave propagates faster, so it triggers the collapse more rapidly, and because each radial layer is denser for the massive cores than for the low-mass cores. Thus, it is important to determine the source of the turbulence present in massive cores, in particular at the size scales traced by NH_3.

6. EFFECTS OF EMBEDDED STARS AND STAR CLUSTERS

6.1. *Individual Stars and Small Groups*

The physical properties of molecular cloud cores, which we are studying now, may be influenced by the interaction of already formed young stellar objects with the surrounding environment. This could be the case especially for the Orion Molecular Cloud which is a well-known active star-forming region, and where stellar winds and outflows may contribute to maintain the amount of energy and pressure observed in Orion dense cores.

Myers et al. (1991) analyzed 61 NH_3 dense cores with embedded *IRAS* sources and concluded that stellar winds alone cannot be responsible for all the observed nonthermal part of the line width, even in cores with luminous stars; they suggested that a mechanism independent of whether the star is present. FM supported this point finding a well defined correlation between the observed nonthermal line width and size ($\Delta v_{obs} \propto R^q$, with $q = 0.4 \pm 0.1$) both in six starless low-mass cores, and in eight cores with an associated star. Therefore, nonthermal motions are part of the initial conditions of the star formation process in such regions on the size scale of observed NH_3 cores.

Myers & Fuller (1993) estimated the effect of stellar winds and outflows on the velocity dispersion of the core gas, assuming that a fixed fraction of the wind momentum flux is coupled into turbulent motions in the core. They found that the wind contribution to the total velocity dispersion exceeds the thermal contribution for $L_* > 400\ L_\odot$, but in no case does the broadening due to winds dominate the total dispersion on the size scale of observed NH_3 cores.

To better compare individual cores we considered the 22 cores in Table 3 where NH_3, CS, and ^{13}CO observations are available (see § 4). In Table 3 the coefficients b and q of the Δv_{NT}–R relation, are listed for every individual massive and low-mass core (see also Figs. 7 and 8 which show the line width–size relation for the individual cores). Eight of the 22 massive cores are associated with an embedded *IRAS* source: Ori B6, Ori B8–9, Ori A6, Ori A9–12, and Ori A15. The far-infrared luminosities (L_{FIR}) can be found in HWW, with the exception of the *IRAS* source in Ori A10, whose luminosity is reported by Anglada et al. (1988), and the one in Ori A11 which is reported by Heyer et al. (1986). Ori B5, Ori B7, and Ori A13 are starless cores, as defined by HWW: they do not contain any *IRAS* source in their HM contour and have been found close to ammonia cores with embedded stellar objects, during the HWW survey. In the other cores, the association with an *IRAS* source is less clear, and we did not consider these cases for the following discussion. The luminosity of *IRAS* sources associated with low-mass cores are listed in BM.

From Table 3 and Figure 7 we note a big variety in the relation between the nonthermal part of the line width and the size especially of individual massive cores, despite of big errors associated with some of the best fits. To estimate the possible influence of the presence of embedded stars in the Δv_{NT}–R relation, we considered the relation between the coefficients b, q, and L_{FIR}, where available. Accounting for the errors associated with b and q, we found very weak correlations between the two quantities. We conclude that from the available data no correlation between the shape of the line width–size relation in a cloud and the luminosity of the embedded stellar object is evident.

HWW mapped in ammonia several cores with embedded stellar objects and in some cases they found other starless cores close to that associated with the *IRAS* source. Comparing the average observed NH_3 line widths in cores associated with a young star ($\langle \Delta v_{obs} \rangle_{star}$) with the average observed NH_3 line widths in the nearest starless cores [$\langle \Delta v_{obs} \rangle_{starless}$], separated by at most 0.5 pc, we obtain an almost identical result:

$$\langle \Delta v_{obs} \rangle_{star} = 0.79 \text{ km s}^{-1} ,$$

$$\langle \Delta v_{obs} \rangle_{starless} = 0.74 \text{ km s}^{-1} .$$

In fact, some of the starless cores studied by HWW have NH_3 line widths broader than the nearby core with an embedded *IRAS* source. In Figure 12 we compare the Δv_{NT}–R relation for the eight massive cores in Table 3 associated with an *IRAS* source, with the Δv_{NT}–R relation in the three massive starless cores as defined by HWW (Ori B5, Ori B7, and Ori A13). The best-fit to the data are

$$\log \Delta v_{NT} = (0.30 \pm 0.05) + (0.32 \pm 0.06) \log R , \quad \mathscr{R} = 0.74 , \quad (19)$$

for massive cores with stars, and

$$\log \Delta v_{NT} = (0.23 \pm 0.09) + (0.20 \pm 0.10) \log R , \quad \mathscr{R} = 0.57 , \quad (20)$$

for massive starless cores. The two relations are very similar considering the relatively high dispersion of the second one, primarily due to the small amount of data used. The similarities in the empirical Δv_{NT}–R relation imply similarities in physical properties for the two categories of cores (see § 5). Taking into account the uncertainties in equations (19) and (20), there is no significant difference between the line width–size relation for massive cores with and without stars, and therefore no significant difference in their derived density pro-

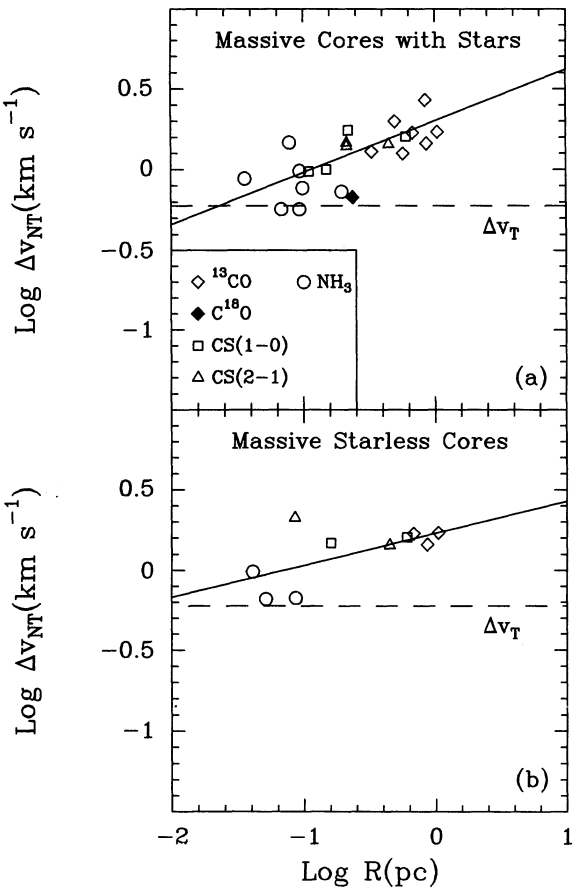

FIG. 12.—Line width–size relation in (*a*) eight Orion massive cores associated with an *IRAS* source, and (*b*) three starless cores in Orion. Dashed lines represent the thermal part of the line width of the molecule of mean mass, assuming temperature 18 K. The two relations do not show any significant difference.

files, pressure profiles, or mass accretion rates. The FIR luminosities of the *IRAS* sources in our sample of massive cores do not exceed 200 $L_\odot$, and most of them are below 50 $L_\odot$. The only exception is the *IRAS* source associated with Ori A6, where $L_{FIR} = 3700\ L_\odot$. For this particular case we note from Table 2B that the ammonia core in Ori A6 has the broadest ammonia line widths of our sample. The luminosity of this embedded source may be high enough to increase the total dispersion of the associated core.

IRAS sources associated with four objects listed in Table 3 have been imaged in the near infrared (*H* and *K'* bands) by Chen & Tokunaga (1994): Ori A9, Ori A10, Ori A12, and Ori A15. In the first three cases, small groupings of near-IR sources, the so-called stellar density enhancements (hereafter, SDEs; Chen 1992), have been discovered. However, the presence of SDEs do not seem to have particular effects in the individual line width–size relations (see Table 3).

We conclude that the presence of an individual star or a small group of stars with luminosity less than 200 $L_\odot$ does not significantly influence the line width–size relations, and the derived physical conditions of the associated molecular cores in our sample.

6.2. *Clusters*

Lada et al. (1991) completed a 2.2 μm survey in the L1630 molecular cloud, where the authors identified four young embedded stellar clusters associated with NGC 2071, 2068, 2064, and 2023. We used these data to study the effects of stellar clusters on nearby dense cores. Five cores of our sample are in the area surveyed by Lada et al. (1991): Ori B5–6, and Ori B7–9. Another core, close to Ori B9 (Ori B9b) mapped in NH_3 by HWW and CS by LBS is contained in the area surveyed at 2.2 μm; this core, discussed in § 2.2.2 for its physical similarities with a low-mass core, is not in Table 2B because it has been mapped just in two different molecular lines, and it is close, but not overlapping, to the ^{13}CO half-maximum contour observed in the Ori B9 cloud (see Fig. 4).

As a first attempt we analyzed how the line width of the ammonia cores are affected by the presence of a nearby stellar cluster; in this case we also included Ori B9b. In § 4, we noticed how ammonia data are important for determining the shape of the line width–size relation, with the strongest difference between massive and low-mass cores being the predominance of nonthermal motions over the thermal ones at the size scales traced by NH_3 (see Fig. 6). Therefore any relation which includes the observed mostly nonthermal line widths (Δv_{obs}) of ammonia lines in massive cores should be reflected in the corresponding line width–size relation. In Table 5 cores considered in this analysis are reported; the observed NH_3 line widths are in column (2); the intercept *b* and the slope *q* in the Δv–*R* relation are in columns (3) and (4), respectively; the correlation coefficient of the Δv–*R* relation is in column (5); in column (6) the star cluster closest in projection to each core is listed; columns (7) and (8) report the number of sources with magnitude at *K* less than 14, in each cluster, as it was found by Lada et al. (1991), and the corresponding luminosity L_K at 2.2 μm. In column (9) there is the projected distance between the peak of the ammonia emission in the HWW maps and the center of the closest cluster, defined by Lada et al. (1991) as

TABLE 5

EMBEDDED STAR CLUSTERS AND NEARBY MASSIVE CORES

Core Name	$\Delta v_{obs}(NH_3)$ (km s^{-1})	*b*	*q*	$\mathscr{R}$	Closest Cluster	Number of Sources[a]	L_K[b] ($L_\odot$)	Distance (pc)
Ori B5	1.0	0.27 ± 0.21	0.11 ± 0.21	0.45	NGC 2071	105	6.1×10^2	0.51
Ori B6	0.8	0.26 ± 0.12	0.30 ± 0.18	0.86				0.80
Ori B7	0.7	0.25 ± 0.05	0.38 ± 0.08	0.96	NGC 2068	192	1.4×10^3	2.12
Ori B8	0.6	0.26 ± 0.06	0.47 ± 0.10	0.96				2.54
Ori B9	0.6	0.20 ± 0.19	0.36 ± 0.25	0.71	NGC 2024	309	2.4×10^3	4.15
Ori B9b[c]	0.3	0.28 ± 0.36	0.75 ± 0.45	0.86				5.05

[a] Number of sources with $m_K < 14$ in each cluster (from Lada et al. 1991).
[b] Luminosity estimates of the clusters at 2.2 μm (see text).
[c] The line width–size relation has been found assuming this core associated with the Ori B9 ^{13}CO cloud (see § 2.2.2).

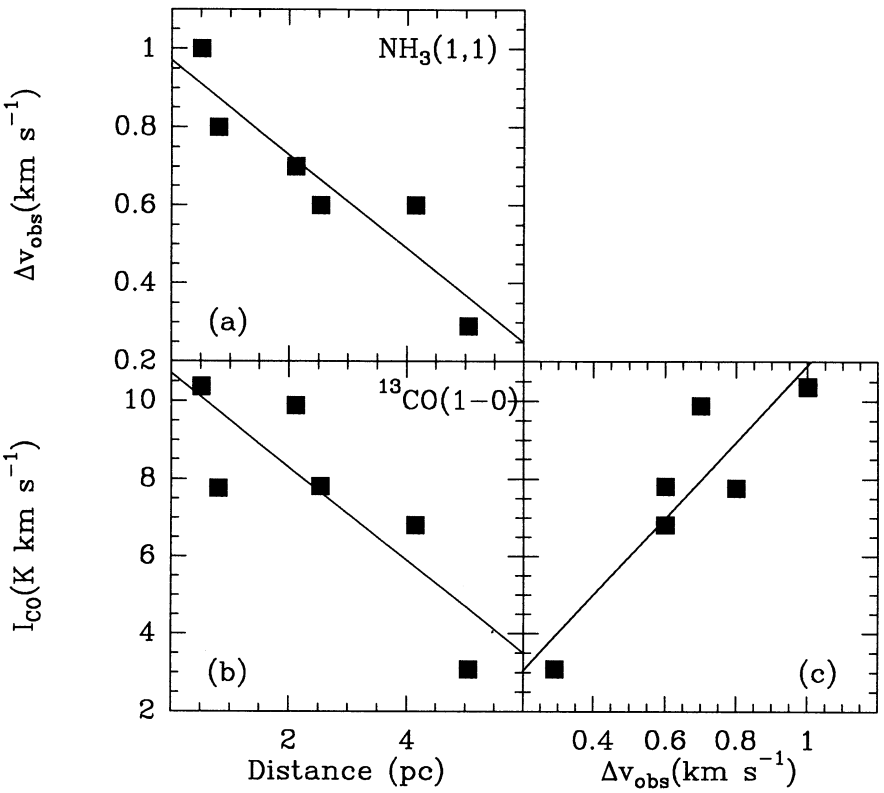

FIG. 13.—(*a*) Observed line width of ammonia cores (HWW) vs. the projected distance between the peak of the ammonia map and the center of the closest star cluster, in Orion B; (*b*) relation between the integrated intensity of ^{13}CO emission at the peak of the same cores and the projected distance from the center of the closest cluster. The information regarding the stellar clusters is provided by the 2.2 μm survey (Lada et al. 1991). (*c*) Relation between the integrated intensity of ^{13}CO emission, proportional to the cloud column density, and the observed line width of embedded ammonia cores. The correlation in the figures appear strong, indicating the importance of stellar clusters in the energy balance of nearby molecular cloud cores.

the peak position in the surface source density distributions. We estimated the luminosity L_K from the cumulative K distributions determined by Lada et al. (1991) for each cluster in Table 5. From these distributions the number of objects in each magnitude bin can be derived. Once we know the magnitude m_K of an object, the estimate of its flux (F_K) is straightforward. Adding together the fluxes at K of each star in the cluster we find the total flux and then the total specific luminosity of the cluster at K (L_K) listed in Table 5. These specific luminosities $L/L_\odot \sim 10^3$ are much greater than the luminosities of the embedded *IRAS* sources in the cores in L1641 and L1630, generally 30–100 $L_\odot$.

Figure 13*a* shows the relation between Δv_{obs} for ammonia cores and the projected distance D from the closest cluster; the best-fit to the data is

$$\Delta v_{obs}(\text{km s}^{-1}) = (0.97 \pm 0.07) - (0.12 \pm 0.02)D\,, \quad \mathcal{R} = -0.93\,. \quad (21)$$

The correlation between these two quantities is very strong: the observed line width of ammonia cores in Orion B, which is primarily nonthermal, as shown in Table 2B, linearly decrease as the distance from a star cluster increases. In Figure 13*b* the relation between the integrated intensity of ^{13}CO emission (I_{CO}) at the peak of NH_3 maps of the same ammonia cores, and the projected distance from a star cluster is shown. The best-fit to the data is given by

$$I_{CO}(\text{K km s}^{-1}) = (10.7 \pm 1.2) - (1.2 \pm 0.4)D(\text{pc})\,, \quad \mathcal{R} = -0.83\,. \quad (22)$$

The quantity I_{CO} is proportional to the column density at the position considered; therefore it is related to the quantity of matter surrounding the dense ammonia core. Relation (22) indicates that column density of gas traced by ^{13}CO, which encloses NH_3 cores, decreases as the distance from a star cluster increases. Equations (21) and (22) imply a relation between I_{CO} and the observed line width of ammonia cores: the lower the ^{13}CO column density, the narrower the line widths of the embedded NH_3 cores. This is shown in Figure 13*c*, where from the best-fit to the data we derive $I_{CO} = (1.1 \pm 1.7) + (9.8 \pm 2.5)\Delta v_{obs}$ with a correlation coefficient $\mathcal{R} = 0.89$. We point out that these relations are based on a relatively few points, and that we also examined the dependence of NH_3 column density on distance and found no significant correlation.

Thus the distance from a young stellar cluster appears to be important in determining the amount of turbulence and pressure inside dense cores. This can be due to mechanical and radiative energy, converted in nonthermal motions, which star clusters furnish to the surrounding molecular cloud cores. This energy, in particular the flux of UV photons driven by the embedded cluster, may also lead to higher fractional ionization in the molecular cloud, increasing the coupling between magnetic fields and the gas.

It is interesting to note that the average NH_3 column density [$\langle N(NH_3)\rangle$] of ammonia cores considered in our analysis, and given by equation (15), does not correlate with the observed NH_3 line width. As equations (21) and (22) show, the amount of molecular material surrounding the core seems to play a more important role in determining the nonthermal broaden-

ing of ammonia lines (see Fig. 13). We can speculatively assume that star clusters may be responsible for the relatively big amount of nonthermal motions and pressure present in nearby massive cores; the gas traced by ^{13}CO, less dense and more uniformly distributed than ammonia, could act as an energetic link between the cluster sites and the surrounding cores.

As we already mentioned, the average density as well as the velocity dispersion in CS cores mapped by Tatematsu et al. (1993) decrease toward the southern part of L1641, therefore increasing the distance from the Orion Nebula, a powerful source of kinetic energy that could drive turbulent motions in the surrounding molecular gas. This scenario has been also considered by Tatematsu et al. (1993) to explain the change in core properties within the Orion A cloud. Another observative evidence of the importance of star clusters in the energy balance of nearby molecular cloud cores could be the line width–size relation found by MF in L1688, a core in the ρ Oph dark cloud associated with an embedded cluster of some 80 stars, essentially a low-mass star cluster with a few massive stars (Wilking, Lada, & Young 1989). In L1688 the nonthermal component of the line width follows the trend $\Delta v_{NT} \propto R^q$, where $q = 0.28 \pm 0.03$, which is very close to the value of q found in Orion cores ($q = 0.21 \pm 0.03$). Therefore, also in this case, the embedded star cluster may have affected the initial structure of the associated core, driving turbulent motions, which have been observed through supersonic molecular line widths at large as well as at small-size scales (Myers et al. 1978; MF).

If star clusters are responsible for changing the energetic contents of nearby star-forming cloud cores, the more quiescent dense cores which lie relatively far from the cluster may be representative of an earlier generation of cores which led to the formation of the stellar population today observed in Orion. As an example, the mostly thermal core Ori B9b (see § 2.2.2) closely resembles a typical low-mass core: the kinetic temperature deduced from ammonia observations is 10 K, the NH_3 line width is ~ 0.3 km s^{-1} (HWW), and the TNT model applied to this core yields density, pressure profiles, and mass accretion rates very similar, within the errors, to low-mass cores, with the nonthermal part of the density profile (eq. [10]) following the trend $n(r) \propto r^{-p}$, with $p = 1.1$ ($p = 1.1$ in low-mass cores; see Table 4). However, this core is ~ 25 times more massive (the NH_3 core has a mass $M = 380\ M_\odot$; HWW) than a typical low-mass core ($M \sim 15\ M_\odot$; Benson & Myers 1989). Ori B9b may be a good candidate to form a group of low-mass stars.

A speculative outline of the cluster history might include the following elements. Consider a massive quiescent cloud which is forming a stellar object. It is possible that after the accretion of a few tenths of a solar mass, the onset of stellar winds and outflows, driven by the young star, started to release mechanical energy into the surrounding cloud core. Because of the large amount of circumstellar mass, the energy input from the central source will gradually increase the internal core pressure and drive turbulent motions without dissipating the core. Whereas quiescent thermal cores can easily smooth out pressure fluctuations, the increased turbulence in the massive circumstellar core may promote fragmentation of the medium, with a possible formation of a small group rather than a single star.

The second generation of cores formed in this model circumstellar cloud would have initial physical conditions characterized by higher internal pressure and turbulence than the original star-forming core. Therefore such cores will have shorter mass accretion times and could form other massive and low-mass stars in timescales of a few times 10^5 yr. To form low-mass stars in massive and turbulent cores the infall must be halted in $\sim 10^5$ yr (or less) after its onset (see Fig. 11). This can probably happen in less massive cores embedded in the cluster cloud, because of the effects of stellar winds and outflows (Lada 1985; Fukui et al. 1986) whose pressure disturbances propagate in a time shorter than t_{exp}, the travel time of the expansion wave (MF).

The formation of stars in the cluster cloud will continue to release kinetic energy into the molecular cloud in the form of observed nonthermal motions and microscopic turbulence. However, the effects of this expanding "energy input" will decrease as the distance from the center of the cluster increases (see eq. [21]) because of the continuous losses of energy which is converted in nonthermal support of molecular cloud cores along the propagation path and because of the density gradient of the cluster cloud. This implies a decreasing star formation efficiency and an increasing fraction of low-mass stars as we move away from the cloud center.

7. SUMMARY

The results presented in this paper are based on molecular line maps from which FWHM line widths and half-maximum contour sizes have been determined. The sample of massive cores studied in this work has been collected from the literature. We observed $^{13}CO(1 \rightarrow 0)$ and $C^{18}O(1 \rightarrow 0)$ lines in selected cores already mapped in NH_3 and CS, and where relatively large-scale information was not available. The observational data range from $R \sim 0.03$ pc to $R \sim 1$ pc, where R is the radius of the half-maximum contour map. The same observed range is available for low-mass cores, after adding new ^{13}CO data to the sample studied by FM. The analysis of massive core physical properties and the comparison with low-mass cores yield the following conclusions:

1. In massive cores: (*a*) the nonthermal component of the line width (Δv_{NT}) follows the trend $\Delta v_{NT} \propto R^q$, where $q = 0.21 \pm 0.03$, value significantly lower than in low-mass cores where $q = 0.53 \pm 0.07$; (*b*) the estimated value of r_{TNT}, the radius at which the thermal and nonthermal components of the line width are equal, is $\sim 7 \times 10^{-3}$ pc, ~ 15 times smaller than in low-mass cores; (*c*) nonthermal motions dominate thermal motions at all observed size scales, and, in particular, at the size scales ~ 0.1 pc traced by ammonia maps, where low-mass cores are primarily thermal.

2. At radius $r = 0.1$ pc, massive cores (*a*) have typical density of 2×10^4 cm^{-3}, ~ 5 times higher than low-mass cores, and have steeper density profiles than low-mass cores; (*b*) have a column density of $\sim 1.5 \times 10^{22}$ cm^{-2}, 5 times bigger than low-mass cores; (*c*) have internal core pressure of $\sim 2 \times 10^{-10}$ ergs cm^{-3}, 20 times higher than in low-mass cores. The higher density and velocity dispersion in massive cores lead to values of infall times for $1\ M_\odot$ of $\sim 7 \times 10^4$ yr, ~ 6 times shorter than in low-mass cores.

3. Only one massive core, Ori B9b, which has not been included in our sample because of lack of data, shows mostly thermal ammonia line widths and kinetic temperature ~ 10 K. This core resembles a typical low-mass core. But Ori B9b is more massive than the typical low-mass core by a factor ~ 25. It has enough mass to form a small stellar group.

4. Visual extinction values of low-mass and massive cores

predicted by the TNT model (3.3 and 16 mag, respectively) are consistent with available observational estimates for similar objects.

5. Physical properties of neighboring starless cores are not significantly different from dense cores associated with embedded young stellar objects, typically having luminosity <200 $L_\odot$. Thus, physical conditions observed in dense cores can be considered part of the initial conditions of the star formation process.

6. The observed line width of ammonia cores in Orion B and the column density of the surrounding ^{13}CO gas both decrease as the distance from the nearest star cluster increases. These trends suggest that luminous ($L/L_\odot \geq 10^3$) embedded clusters may influence their nearby gas and cores increasing their velocity dispersions through their mechanical and radiative luminosity, and perhaps through changes in cloud pressure.

7. The TNT model is able to reproduce observed trends in the line width–size relation, proving the internal consistency of model and Δv–R data.

We thank the personnel of Haystack Observatory and FCRAO and those who helped with the observations including Peter Barnes, Mark Heyer, and Nimesh Patel. We are grateful to Peter Barnes, José F. Gomez, Joel Kastner, and Daniel Puche for their help during data reduction. We thank Y. Fukui and A. Mizuno for communicating data in advance of publication. We thank the referee for many constructive comments and suggestions. We thank John Holliman and Chris McKee for helpful discussions. P. C. acknowledges the support of the Universitá di Bologna, and a Smithsonian Astrophysical Observatory Predoctoral Fellowship.

APPENDIX A

CONSISTENCY OF TNT MODEL WITH LINE WIDTHS AND MAPS OF SINGLE AND MULTIPLE LINES

In § 4 we showed the line width–size relations in massive and low-mass cores (eqs. [7] and [8], and Fig. 6). As we already pointed out, each core included in the previous relations has been mapped in at least three different molecular tracers of gas density. The line width of the mean molecule increases as the density drops from $n \sim 10^4$ cm^{-3} (value traced by NH_3) to $n \sim 10^3$ cm^{-3} (value traced by ^{13}CO). This effect can be seen more clearly from Figures 7 and 8, where the Δv_{NT}–R relations of individual cores are shown.

Starting from this observational evidence we then deduced the variation of density and pressure with the radius of the cores, modeled as TNT spheres, i.e., spheres in hydrostatic equilibrium where the velocity dispersion accounts both for thermal and nonthermal motions of the gas particles (eq. [9]).

Starting from the TNT models (§ 5) we now test the self-consistency of the TNT model and the data it uses. We make predictions about the variation of observed line widths of a single species as a function of b, the projected distance from the center of the cloud. Assuming Gaussian molecular lines, we can write the density profile as a function of b and v_z, the velocity component of the observed molecular species along the line-of-sight, in the form (see eq. [10] and § 5 for an explanation of the symbols):

$$n(z, v_z) = \frac{\sigma_T^2}{2\pi G m r_0^2} (x^{-2} + x^{-p}) \frac{1}{\sqrt{2\pi}\sigma} \exp\left[-v_z^2/(2\sigma^2)\right] , \tag{A1}$$

where $x \equiv r/r_0 = [(b^2 + z^2)/r_0^2]^{1/2}$; σ is given by equation (9) and $\sigma_{NT} = c(b^2 + z^2)^{q/2}$ (c is known from observations). Note that this "density profile" $n(z, v_z)$ has dimensions of density per unit velocity. At the peak of the line ($v_z = 0$), expression (A1) becomes

$$n(z, 0) = \frac{\sigma_T^2}{2\pi G m r_0^2} (x^{-2} + x^{-p}) \frac{1}{\sqrt{2\pi}\sigma} . \tag{A2}$$

Integrating equation (A1) along the line-of-sight z, we obtain the column density as a function of b and v_z:

$$N(b, v_z) = \int_0^{z_{max}} n(z, v_z) dz . \tag{A3}$$

At the peak of the line:

$$N(b, 0) = \int_0^{z_{max}} n(z, 0) dz , \tag{A4}$$

where

$$z_{max} = (R_b^2 - b^2)^{1/2} . \tag{A5}$$

In the equation (A5), R_b is the "boundary radius," defined to be 2 times the half-maximum radius of the map in the observed species (NH_3, CS, $C^{18}O$, or ^{13}CO). The density at the boundary radius, n_b, can then be found from equation (10), substituting n with n_b and r with R_b. The values of derived boundary densities and radii for low mass and massive cores are listed in Table 6. The density values reported in Table 6 are less by a factor 4–50 than the critical densities, calculated by equating the collisional excitation rates to the corresponding transition Einstein A-value, and assuming optically thin emission. This difference reflects the effects of line optical depth and unresolved structure inside the map.

TABLE 6

BOUNDARY RADII AND DENSITIES FOR MASSIVE AND LOW-MASS CORES

MOLECULE	n_b (cm^{-3})		R_b (pc)	
	Low Mass	Massive	Low Mass	Massive
NH_3	1.4×10^3	5.3×10^3	0.16	0.18
$C^{18}O$ or CS[a].....	3.5×10^2	9.6×10^2	0.38	0.50
^{13}CO	7.1×10^1	1.7×10^2	1.2	1.44

[a] $C^{18}O$ data have been used for low mass cores. For massive cores we use CS data, because of the lack of $C^{18}O$ data in our massive core sample (see Table 2B).

To find the model FWHM line width Δv at a certain value of b, we define $v_{z,1/2}$ by

$$\frac{N(b, v_{z,1/2})}{N(b, 0)} = \frac{1}{2}. \tag{A6}$$

The above expression has been solved numerically (for $b/R_b = 0.1, 0.2, \ldots, 0.9$) integrating equations (A3) and (A4) and taking the ratio. From equation (A6) we obtain $v_{z,1/2}$, then $\Delta v = 2\, v_{z,1/2}$. Δv is the line width of the mean molecule; to find the line width of the observed species i we use the expression:

$$\Delta v_{\rm obs}(i)^2 = \Delta v^2 + 8 \ln 2 (kT) \left(\frac{m - m_i}{m m_i} \right), \tag{A7}$$

where $m = 2.33$ amu is the mass of the mean molecule. For each species i, a relation between $\log \Delta v_{\rm obs}(i)$ and $\log b$ has been found using a least-squares fit to the model data. The intercept b' (not to be confused with the projected radius b) and slope q of the $\log \Delta v_{\rm obs}(i)$–$\log b$ relation are listed in Table 7. The listed numbers give the predicted variations of line width with projected radius for the three molecular tracers.

We note from Table 7 the shallow slope in the variation of ammonia line width in low-mass cores, $q = 0.33$, as compared with the slope of the fit to all data, $q = 0.44$, which coincides with the value of q found by Fuller & Myers (1992) in low-mass cores. Although observed NH_3 line widths are predicted to increase with the projected radius b, we expect to see a shallower slope q than in the $\Delta v_{\rm obs}$–b relation found from different density tracers. From Table 7, we see that this is a general trend, with low-mass ammonia cores being the extreme case. This is probably due to the fact that at the size scale of low-mass ammonia cores, the nonthermal contribution to the velocity dispersion is small (see § 4). Moreover, the thermal velocity dispersion does not depend upon radius, as we initially assumed. Therefore, the resultant variation of NH_3 line width with projected radius is small and significantly shallower than the general $\Delta v_{\rm obs}$–b relation where different density tracers have been used.

We now consider how closely the TNT model can reproduce the observed $\Delta v_{\rm NT}$–R relations (see Fig. 6 and eqs. [7] and [8]), and how the $\Delta v_{\rm NT}$–R relation depends upon the value of projected radius chosen to delineate the map contour.

To answer these questions we first calculate nonthermal line widths starting from the previously calculated line width of the molecule of mean mass Δv, using the expression:

$$\Delta v_{\rm NT}^2 = \Delta v^2 - 8 \ln 2 \left(\frac{kT}{m} \right). \tag{A8}$$

Following the method used for observed line widths, expression (A8) has been applied to all values of Δv calculated from (A1) for $b/R_b = 0.1, 0.2, \ldots, 0.9$, and for each value of critical density. Figure 14 gives a global picture of model results. All the data calculated with the above method are plotted together for massive (Fig. 14*a*) and low-mass (Fig. 14*b*) cores. Each species has its own symbol. The filled symbols mark the value of $\Delta v_{\rm NT}(i)$ at which $b = 0.5\, R_b$. Thin lines are least-squares fits to all the data points in the figures; the corresponding values of b' and q are in Table 8 (fourth row). The model best-fit line is compared with the best-fit to the observed data points (dashed lines) shown in Figure 6 (see eqs. [7] and [8]). Note the close agreement between the predicted and observed fit.

TABLE 7

INTERCEPT AND SLOPE OF THE $\Delta v_{\rm obs}$-b RELATION IN MASSIVE AND LOW-MASS CORES

SPECIES	LOW-MASS		MASSIVE	
	b'	q	b'	q
NH_3	0.04 ± 0.01	0.33 ± 0.01	0.20	0.15
$C^{18}O$ or CS.....	0.12 ± 0.01	0.37 ± 0.01	0.22	0.16
^{13}CO	0.20	0.41 ± 0.01	0.24	0.16
Total.....	0.18 ± 0.01	0.44 ± 0.01	0.24	0.18

NOTE.—Negligible errors (< 0.005) are not reported in the table.

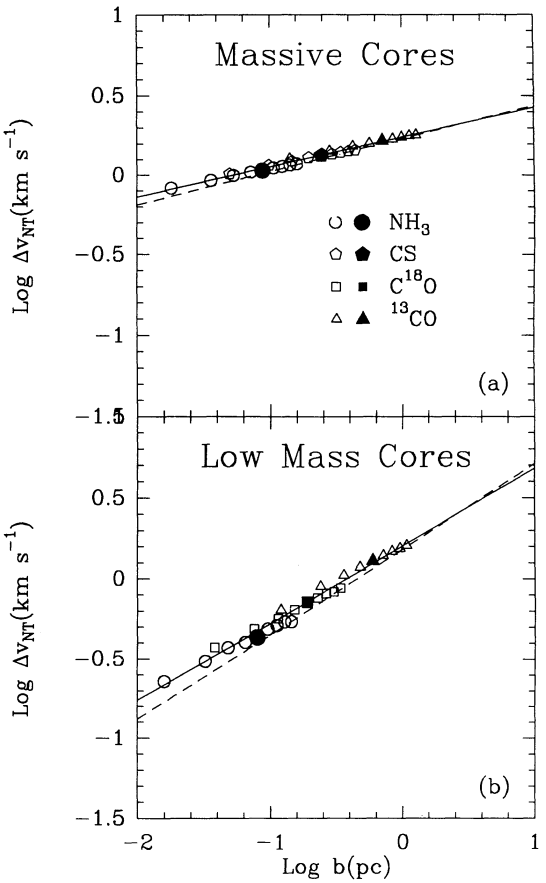

FIG. 14.—Nonthermal line widths of NH_3, CS, $C^{18}O$, and ^{13}CO as a function of projected radius b, for (*a*) massive and (*b*) low-mass cores, as predicted by the TNT model (see Appendix). For each species, Δv_{NT} values have been calculated for $b/R_b = 0.1, 0.2, \ldots, 0.9$, where R_b is the boundary radius. Straight lines represent least-square fits to the model data in the figures. Dashed lines are best-fit lines to the observed data points shown in Fig. 6. Note the close agreement between the fit to model and observed data. The intercept and slope of the best-fit lines are listed in Table 8. Filled symbols mark the value of Δv_{NT} at which $b = 0.5\ R_b$.

In Table 8 we report intercepts b' and slopes q of the log Δv_{NT}–log b relations in low-mass and massive cores, found by least-square fits to the model data. In Table 8 we also list b' and q relative to least-square fits to only three data points: one for each density tracer at a specific value of b/R_b. We note that all values of b' and q reported in Table 8 are consistent with the corresponding intercept and slope found from the observed relations (shown for comparison in the last row of Table 8). This proves the consistency of the TNT model, which is able to reproduce observed trends in the line width–size relation. Moreover, we see from Table 8 that the Δv_{NT}–R relation should not depend upon the assumed definition of core radius, as long as the same definition is applied to all molecular tracers. Our choice of the half-maximum map contour as radius of the core is therefore a valid one. Although it is an arbitrary choice, choosing a different contour level would not affect the conclusions of this paper.

In a future paper, we plan to include excitation and optical depth effects in our model. Then, the TNT model can be used to make more accurate predictions about the spatial distribution and line width of the emission from each molecule.

TABLE 8

INTERCEPT AND SLOPE OF THE Δv_{NT}-b RELATION IN MASSIVE AND LOW-MASS CORES

	Low Mass		Massive	
b/R_b	b'	q	b'	q
0.2	0.29 ± 0.01	0.54 ± 0.01	0.27 ± 0.01	0.21 ± 0.01
0.5	0.23 ± 0.01	0.54 ± 0.02	0.25	0.21
0.8	0.19 ± 0.01	0.52 ± 0.01	0.24	0.21
Total	0.20 ± 0.01	0.48 ± 0.01	0.24	0.19 ± 0.01
Observed.....	0.18 ± 0.06	0.53 ± 0.07	0.23 ± 0.03	0.21 ± 0.03

NOTE.—Negligible errors (< 0.005) are not reported in the table.

REFERENCES

Anglada, G., Rodriguez, L. F., Torrelles, J. M., Estalella, R., Ho, P. T. P., Canto, J., Lopez, R., & Verdes-Montenegro, L. 1989, ApJ, 341, 208
Bally, J. 1989, in IAU Colloq. 120, Structure and Dynamics of the Interstellar Medium, Lecture Notes in Physics, Vol. 350, ed. G. Tenorio-Tagle, M. Moles, & J. Melnick (Berlin: Springer), 309
Bally, J., Langer, W. D., Stark, A. A., & Wilson, R. W. 1987, ApJ, 312, L45
Bartla, W., Wilson, T. L., Bastien, P., & Ruf, K. 1983, A&A, 128, 279
Baud, B., & Wouterloot, J. G. 1980, A&A, 90, 297
Benson, P. J., Caselli, P., Myers, P. C., & Goodman, A. A. 1994, in ASP Conf. Ser. Vol. 65, Clouds, Cores, and Low-Mass Stars, ed. D. P. Clemens & R. Barvainis (San Francisco: ASP), 67
Benson, P. J., & Myers, P. C. 1989, ApJS, 71, 89
Bertoldi, F., & McKee, C. F. 1992, ApJ, 395, 140
Brand, J., & Wouterloot, J. G. A. 1991, ESO Sci. Rep. Ser., 11, 1
Caselli, P., & Myers, P. C. 1994, in ASP Conf. Ser., Vol. 65, Clouds, Cores, and Low-Mass Stars, ed. D. P. Clemens & R. Barvainis (San Francisco: ASP), p. 52
Castets, A., Duvert, G., Dutrey, A., Bally, J., Langer, W. D., & Wilson, R. W. 1990, A&A, 234, 469
Cernicharo, J., & Bachiller, R. 1984, A&AS, 58, 327
Cernicharo, J., Bachiller, R., & Duvert, G. 1985, A&A, 149, 273
Cesaroni, R., & Wilson, T. J. 1994, A&A, 281, 209 (CW)
Chandrasekhar, S. 1939, Stellar Structure (Chicago: Univ. of Chicago Press)
Chen, H. 1992, Ph.D. thesis, Univ. of Hawaii
Chen, H., Fukui, Y., & Iwata, T. 1993, ApJ, 411, 239
Chen, H., Fukui, Y., & Yang, 1992, ApJ, 398, 544
Chen, H., & Tokunaga, A. T. 1994, ApJS, 90, 149
Cohen, R. J. Matthews, N., Few, R. W., & Booth, R. S. 1983, MNRAS, 203, 1123
Dutrey, A., Langer, W. D., Bally, J., Duvert, G., Castets, A., & Wilson, R. W. 1991, A&A, 247, L9
Erickson, N. R., Goldsmith, P. F., Novak, G., Grosslein, R. M., Viscuso, P. J., Erickson, R. B., & Predmore, C. R. 1992, IEEE Trans. on Microwave Theory and Techniques, 40, 1
Fukui, F., & Mizuno, A. 1992, private communication
Fukui, Y., Sugitani, K., Takaba, H., Iwata, T., Mizuno, A., Ogawa, H., & Kawabata, K. 1986, ApJ, L85
Fukui, Y., Takaba, H., Iwata, T., & Mizuno, A. 1988, ApJ, 325, L13
Fuller, G. A., & Myers, P. C. 1992, ApJ, 384, 523 (FM)
Genzel, R., & Stutzki, J. 1989, ARA&A, 27, 41
Goldsmith, P. F., Margulis, M., Snell, R. L., & Fukui, Y. 1992, ApJ, 385, 522
Goodman, A. A., Crutcher, R. M., Heiles, C., Myers, P. C., & Troland, T. H. 1989, ApJ, 338, 161
Green, D. A. 1991, MNRAS, 253, 350
Harju, J., Walmsley, C. M., & Wouterloot, J. G. A. 1993, A&AS, 98, 51 (HWM)
Heyer, M. H., Snell, R. L., Goldsmith, P. F., Strom, S. E., & Strom, K. M. 1986, ApJ, 308, 134
Ho, P. T. P., Martin, R. N., Myers, P. C., & Barrett, A. H. 1977, ApJ, 215, L29
Hodapp, K. W., & Deane, J. 1993, ApJS, 88, 119
Holliman, J. H., & McKee, C. F. 1995, in preparation
Iwata, T., Fukui, Y., & Ogawa, H. 1988, ApJ, 325, 372 (IFO)
Lada, C. J. 1985, ARA&A, 23, 267
Lada, E. A., Bally, J., & Stark, A. A. 1991, ApJ, 368, 432 (LBS)
Lada, E. A., DePoy, D. L., Evans, II, N. J., & Gatley, I. 1991, ApJ, 371, 171
Larson, R. B. 1981, MNRAS, 194, 809
Maddalena, R. J., Morris, M., Moscowitz, J., & Thaddeus, P. 1986, ApJ, 303, 375
Myers, P. C., & Fuller, G. A. 1992, ApJ, 396, 631 (MF)
———. 1993, ApJ, 402, 392
Myers, P. C., Fuller, G. A., Goodman, A. A., & Benson, P. J. 1991, ApJ, 376, 561
Myers, P. C., & Goodman, A. A. 1988, ApJ, 329, 392
Myers, P. C., Ho, P. T. P., Schneps, M. H., Chin, G., Pankonin, V., & Winnberg, A. 1978, ApJ, 220, 864
Myers, P. C., Ladd, E. F., & Fuller, G. A. 1991, ApJ, 372, L95
Pastor, J., Estalella, R., Lopez, R., Anglada, G., Planesas, P., & Buj, J. 1991, A&A, 252, 320
Patel, N. A., Xie, T., & Goldsmith, P. F. 1994, ApJ, 413, 593
Shu, F. H. 1977, ApJ, 214, 488
Snell, R. L. 1980, ApJS, 45, 121
Snell, R. L., Scoville, N. Z., Sanders, D. B., & Erickson, N. R. 1984, ApJ, 284, 176
Strom, K. M., Margulis, M., & Strom, S. E. 345, L79
Sugitani, K., Fukui, Y., Ogawa, H., & Kawabata, K. 1986, ApJ, 303, 667 (SFOK)
Takano, T., Stutzki, J., Fukui, Y., & Winnewisser, G. 1986, A&A, 167, 333
Tatematsu, K., et al. 1993, ApJ, 404, 643 (TUKH)
Ungerechts, H., Walmsley, C. M., & Winnewisser, G. 1986, A&A, 157, 207 (UWW)
Van Gorkom, J. H., & Ekers, R. 1991, in ASP Conf. Ser., Vol. 6, Synthesis Imaging in Radio Astronomy, ed. R. A. Perley, R. F. Schwab, & & A. H. Bridle (San Francisco: ASP), 338
Wilking, B. A., Lada, C. J., & Young, E. T. 1989, ApJ, 340, 823
Wootten, A., Loren, R. B., Sandqvist, A., Friberg, P., & Hjalmarson, A. 1984, ApJ, 279, 633
Zhou, S., Evans, II, N. J., & Mundy, L. G. 1990, ApJ, 355, 159 (ZEM)